Anisotropy Distributions in Nanoparticles For Magnetic Hyperthermia Applications

David Carlos Lloyd

Master of Science by research

University of York

Physics

January 2015

Abstract

A model of magnetic hyperthermia for which hysteresis heating is the dominant mechanism is presented in the context of medical applications. A ferrofluid is characterised physically and magnetically. TEM images are used to calculate a shape anisotropy distribution and the effect of distributed anisotropy on hysteresis heating is demonstrated. Temperature decay of remanence measurements are then presented for an indirect calculation of the median blocking temperature and the effective anisotropy.

Table of Contents

List of Figures:

Acknowledgements

There are many that I wish thank for their contributions, insights and support during my MSc. Firstly, I would like to thank Liquids Research Ltd. for funding and for the samples used in this work. From Liquids Research I would like to thank Dr. James Timmis for using the magnetherm and for obliging all of my ferrofluid related requests. I would also like to thank Dr. Mannan Ali and Dr. Oscar Cespedes from The University of Leeds for support when using the low temperature VSM.

I would like to say a big thank you to the past and current members of the Magnetic Materials Research Group at the University of York for making me feel so welcome. Specifically, fellow students Teodor Huminiuc and Ioan Polenciuc for the constant laughs, awkwardness, food and Romanian music. Furthermore, to Oliver Whear for support, encouragement and some fantastic times.

I must thank my family for their constant support and encouragement. They have always been there for me, believed in me and kicked my arse when necessary.

Finally, I would not have made it anywhere near this far without the my two supervisors: Dr. Gonzalo Vallejo-Fernandez and Prof. Kevin O'Grady. Over the past year they have been my constant motivation, inspiration and a source of some of the most, eccentric, stories I've ever heard.

This thesis is dedicated to my grandfather, A. G. Lloyd (1917-2014).

Declaration:

I declare that the work presented in this thesis is based purely on my own research, unless otherwise stated, and has not been submitted for a degree in this or any other university.

Chapter 1: Introduction

Ferrofluids are colloidal suspensions of nano-scale magnetic particles. The carrier fluid can be water or be oil based. The particles are usually coated by a layer of surfactant that reduces or eliminates the aggregation due to magnetic or dipole attraction between particles. Ferrofluids offer the ability to magnetically control a liquid. This provides a wide range of commercial and technological applications, for example nearly frictionless liquid seals for rotating mechanical systems.

Ferrofluids can be functionalised by attaching or encasing the magnetic particles with other substances. This has received much attention in recent years for medical applications such as: targeted drug delivery and magnetic hyperthermia.

Magnetic hyperthermia is the heating observed in magnetic nanoparticles in the presence of an alternating magnetic field. Therefore, ferrofluids can provide localised heating for the treatment of certain cancers. Magnetic hyperthermia for this application is the motivation for this thesis.

At present, several treatments in combination are used to treat cancer. As an illness, cancer has no established effective treatment protocol for which there is negligible damaging side effects and a high rate of success. The current standard treatments for cancer include surgery, chemotherapy, and radiotherapy. Research is being conducted to create new treatment options. These include immunotherapy and thermotherapy. Thermotherapy is any treatment method which exploits the lowered heat resistance of cancerous tissues compared with that of normal tissues. Cancerous tissues undergo cell death even in the temperature range of 42 to 43°C. Thus, thermotherapy is a promising potential treatment for cancer [1]. Magnetic hyperthermia is a theoretically viable route to thermotherapy.

Iron oxide nanoparticles for use as an MRI contrast agent have already been studied and have been approved for intravenous injection. DeNardo et al. injected iron oxide nanoparticles conjugated with monoclonal antibodies into mouse tails and found that they can be made to accumulate in tumors [2].

Wust et al. showed that injecting high concentrations of magnetic nanoparticles directly into tumors at known locations and irradiating them with an alternating magnetic field caused the local temperature of the tumors to increase [3]. Therefore, it is known that iron oxide nanoparticles are safe for medical use, can be directed to a tumor in vivo and can provide localized heating.

Hyperthermia for medical applications requires a multidisciplinary approach. Drug and particle delivery is primarily a biochemical consideration and the treatment of cancer a medical one. Physics, specifically magnetic and materials research, focuses on improving the heating performance of magnetic nanoparticles.

In order for magnetic hyperthermia to be used as a standard medical treatment a complete physical model of the heating and the heating system is required. First, the particles in the ferrofluids used have been the subject of much consideration. The effects of dipole-dipole coupling in many particle systems are not yet fully understood ([4], [5], [6], [7]). However, it is known that a ferrofluid becomes unstable if the size of the dipole-dipole coupling between the closest nanoparticles is more than five times the thermal energy [4], [7]. Most nano-scale particles are sufficiently small enough to cross the tissue barrier in human bodies (order of micrometers). However, the effect of the dipole-dipole coupling limits the upper size of the particles that can be used and the profile of the particle dispersion. Further considerations for the particles are needed due to clustering effects. These can be agglomeration, aggregation, or flocculation and may occur in ferrofluids depending on the surface charge of biofunctionalized nanoparticles or on the interaction between tumor-targeting ligands.

Many magnetic properties and so the heating mechanisms in the hyperthermia systems are dependent on the nanoparticle size. For these reasons, a large number of studies have focused on controlling the size, shape or composite structure of nanoparticles to optimize the heating from hyperthermia. Since then, researchers have focused on developing methods to synthesize well-controlled nanoparticles. These have been reviewed extensively in the literature [8], [9].

Since treatment is a medical issue, physical models must pay consideration to guidelines set out by medical institutions. For example, the International Commission on Non-Ionizing Radiation Protection [10], imposes an upper limit for amount of exposure to localized heating. This further demonstrates the extent of the multidisciplinary nature of medical hyperthermia.

Clinical trials are already being conducted on human beings and magnetic nanoparticles have been shown to reduce tumor size [11]. This is remarkable considering that the combination of nanoparticles and the magnetic oscillation equipment have not been optimized yet [12], [13].

If a complete model of hyperthermia were to be understood, then predictable heating could be achieved in patients. At this point thermotherapy via magnetic hyperthermia could be established as a standard cancer treatment method to reduce the disease burden of a cancer patient.

The conclusion of what has been mentioned thus far is that many advances have been made in the study of magnetic hyperthermia for medical applications. However, there is still a long way to go before it is viable. Despite the advances made, the exact nature of the heating mechanisms are not yet fully understood [14]. A model of magnetic hyperthermia is presented by the magnetic materials group at the University of York; this is discussed in chapter 3. This model predicts that the dominant mechanism of heat generation in vivo is hysteresis heating.

The heat generated by a system of magnetic nanoparticles is strongly dependent on the size of the magnetic anisotropy constant. In a real ferrofluid system containing a distribution of elongated magnetic particles, there will exist a distribution of the magnetic shape anisotropy.

The experimental work carried out in this thesis was the development of a method for measuring the shape anisotropy distribution from transmission electron micrographs. This was conducted assuming a shape dominated anisotropy. This assumption was considered in the context of magnetic measurements. Namely, temperature decay of remanence measurements. The outcome provides the necessity for theoretical models of magnetic hyperthermia to include the effect of distributed anisotropy on the heating.

Before beginning the thesis it is necessary to note the unit system involved. In general, the magnetic research community operates in the c.g.s unit system rather than SI. Most literature assumes the use of this system. Therefore, c.g.s. units are assumed for all mathematical relationships used in this work.

Chapter 2: Fine Particle Magnetism

This experimental work described in this thesis is conducted on ferrofluids. It is useful to discuss the magnetic principles involved before a model of magnetic hyperthermia is discussed. This chapter does this in the context of fine particle systems, such as those found in magnetic liquids.

The chapter starts with the theory of single domain particles and the reversal mechanisms involved. These two concepts are then discussed with regard to the Stoner-Wohlfarth model. Secondly, dynamic principles such as thermal activation of magnetisation and frequency dependant hysteresis are discussed. Finally, these contributions are brought together in terms of an energy barrier distribution for the systems investigated herein.

2.1 Single Magnetic Domains:

Magnetic domains were first proposed by Weiss [15] in order to explain the existence of bulk magnetic materials in a demagnetised state. A domain consists of a region in a material where all of the spin magnetic moments are spontaneously aligned parallel to each other. Therefore, a multi-domain magnetic material can be observed to have zero net magnetisation when the internal domains are ordered randomly with respect to each other. This is referred to as a flux closure configuration of domains. Domains are formed in order to reduce the overall magnetostatic energy of the material, which is defined by equation 2.1.

$$E_{MS} = \frac{1}{2} N_d M^2 \tag{2.1}$$

Where N_d is a shape demagnetising factor and M is the magnetisation of the material.

Without the existence of magnetic domains, materials would exhibit large stray fields. In multi-domain structures, domains organise themselves so as to reduce the magnitude of the stray field and therefore the overall magnetostatic energy of the material. Domains are separated by domain walls. Domain walls are areas of a material where the spin magnetic moments gradually rotate to orientate themselves parallel to that of the neighbouring domain. Since domain walls contain spins that are not parallel to each other there is an energy contribution associated with the presence of a domain wall. When the width of a domain wall and the size of the material become comparable to each other, i.e. in fine particle systems, the energy added to the system by the creation of a domain wall becomes greater than the reduction of the magnetostatic energy caused by the formation of multiple domains. At this point it is no longer energetically favourable for the material to form multiple domains. This behaviour was predicted by Frenkel in 1930 [16] and single domain particles were observed by Elmore in 1938 [17]. The structure of single and multiple domain materials is shown below in figure 2.1.

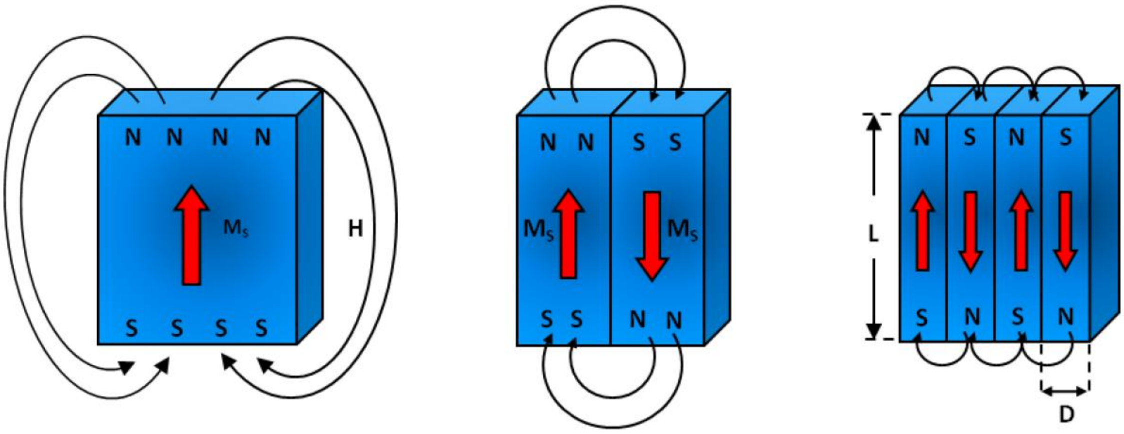

Figure 2.1: Schematic of single and multi-domain structures showing the reduction in stray field.

The critical size for single magnetic domain particles was investigated by Kittel [18]. The critical size for a cubic crystal to transition to a multi-domain state can be estimated by equating the energy of the multi-domains state with that of the single domain state. This relation is shown by equation 2.2 and is a reasonable approximation for most materials.

$$L_c = \frac{1.7\gamma_D}{\pi M_S} \tag{2.2}$$

Where L_C is critical crystal length, M_S is the saturation magnetisation and γ_D is the domain wall energy. For magnetite the critical size has been found to be approximately 15nm [19]. It should be noted that elongated particles have lower magnetostatic energy because the shape demagnetising factor is smaller along the elongation axis. This means that elongated particles of a greater volume can retain their single domain state compared to spherical particles.

Since single domain particles do not have domain walls, magnetisation reversal cannot take place via domain wall motion. This means that the magnetisation vector can only reverse by overcoming an anisotropy energy barrier.

2.2 Reversal Mechanisms:

2.2.1 Magnetisation Reversal:

Magnetisation reversal is the process which leads to the magnetisation vector within a material orientating itself 180° with respect to its initial direction (uniaxial case). This represents the change of magnetisation from one stable orientation to another. The reversal mechanisms discussed in this section are those in the presence of an applied magnetic field however, other routes to reversal do exist. The magnetisation vector can reverse by multiple methods; these are usually classified as either coherent or incoherent. Coherent reversal is when the spin magnetic moments of all the atoms in a material are orientated parallel to each other and remain parallel to each other during the reversal process. Incoherent reversal is when they do not remain parallel during the reversal process but become parallel by the end of the process. An example of coherent and incoherent reversal can be seen in figure 2.2. Paramagnetic materials and diamagnetic materials reverse their magnetisation by coherent means. Materials that exhibit ferromagnetic activity can also undergo reversal by coherent means or by incoherent means depending on their size. The exact mechanism by which a material undergoes reversal depends on the material itself, its size and shape and magnetic anisotropies involved.

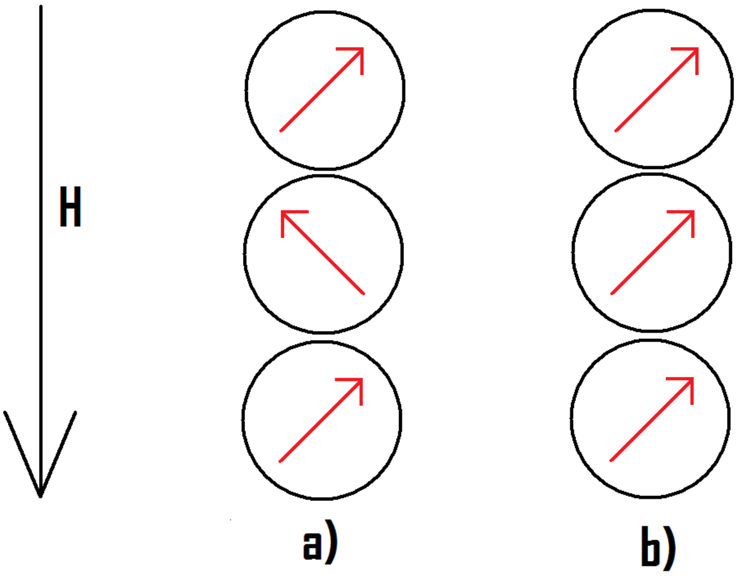

Figure 2.2: Single domain particles reversing in an external field a) incoherently and b) coherently.

Examples of incoherent reversal relevant in fine particle systems are magnetisation fanning and magnetisation curling. Magnetisation fanning [20] is shown in figure 2.2a, in which the magnetisation vectors of successive adjacent particles fan out in a plane by rotating in alternate directions. The fanning mechanism is favoured over coherent reversal because the external field must overcome a lower energy barrier for reversal. This is because the fanning of alternate particles brings the north and south poles closer together. Thus, the extent of the stray field and consequently the total magnetostatic energy is reduced. It should be noted that the fanning mode occurs in systems of many particles and the spins within each individual particle rotate by coherent reversal. Additionally, the exchange energy need only be considered when the point of contact between the particles is considered large. When the point of contact between two particles becomes large the number of non-parallel spins becomes large and the exchange forces favour coherent reversal.

Another mechanism of incoherent reversal is curling, shown in figure 2.3a. During a curling reversal all of the spins in a cross section, perpendicular to an applied field, rotate incoherently such that in each cross section they form flux closure configurations. Since every cross section consists of spins that form partial or full flux closure configurations, there are few free poles and the magnetostatic energy is minimised. There is an energy contribution from the exchange interaction since the spins in each cross section are not parallel.

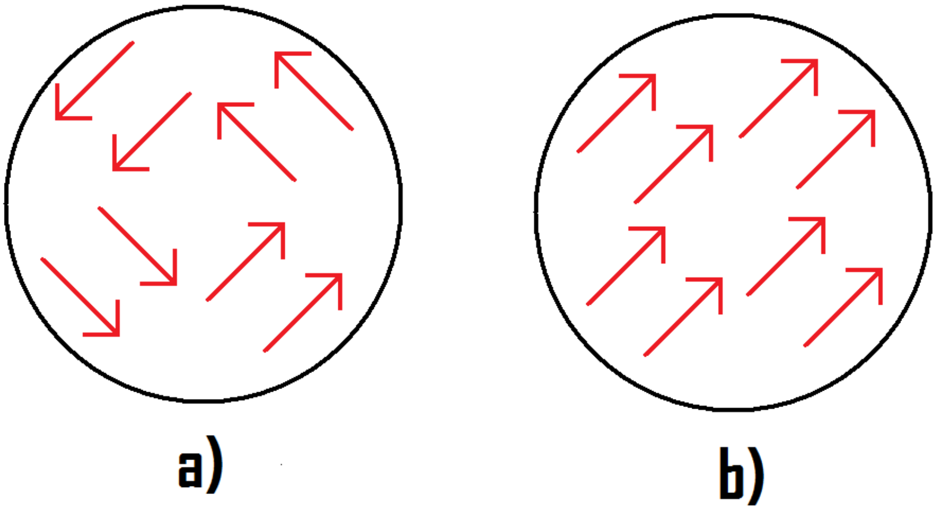

Figure 2.3: Cross section of a particle undergoing reversal by a) curling and b) coherent reversal. The external field is applied into the page.

There is a size dependence associated with the mechanism of reversal. Small particles reverse by coherent rotation. As particles increase in size the magnetostatic energy associated with each particle due to the free poles increases. Indeed this energy is directly proportional to the particle volume [21]. Therefore, the energy barrier to reversal becomes greater. Larger particles reverse by curling because the mean angle between adjacent spins in a given cross section is reduced. Thus, the exchange energy per unit volume of the particle becomes smaller with bigger particles. Magnetisation reversal occurs by the mechanism with the lowest energy barrier, in small particle the energy barrier due to magnetostatic energy for coherent reversal is less than the exchange energy required for the curling mode. Therefore, coherent reversal is preferred in small particles. In nanoparticles of the order of 10nm, the particles reverse by coherent means.

2.2.2 Magnetic Reversal in the Liquid State:

Due to the colloidal nature of ferrofluids there are two further mechanisms for magnetisation reversal associated with the liquid state. The first of these is Néel relaxation [22], this mechanism occurs when the magnetisation vector rotates with respect to the particle while the particle itself remains stationary. There is a relation time associated with Néel relaxation, this relaxation time is related to the superparamagnetic nature of the particles and is give by equation 2.3.

$$\tau_N^{-1} = f_0 exp\left[-\frac{KV}{K_B T}\right] \tag{2.3}$$

Where K is the magnetic anisotropy, V is the particle volume, KB is the Boltzmann factor, T is the temperature and f_0 is a frequency factor (usually taken as $f_0=10^9$ Hz).

The second reversal mechanism in the liquid state is Brownian rotation. Here, the magnetisation vector remains stationary with respect to the particle and the particle physically rotates taking the magnetisation vector with it. There is a relaxation time associated with Brownian rotation as well and is given by equation 2.4 [23]. Where η is the viscosity of the carrier liquid.

$$\tau_B = \frac{3V\eta}{K_B T} \tag{2.4}$$

At a constant temperature the mechanism of reversal depends on the volume of the particle. Smaller particles reverse by Néel rotation and large particle reverse predominantly by Brownian rotation. The critical diameter that marks the transition between Néel rotation and Brownian rotation can be determined by equating the two relaxation times and solving for the particle diameter. This gives equation 2.5.

$$D_S = \left[\frac{24K_B T}{\pi K}\right]^{\frac{1}{2}} \tag{2.5}$$

Using the bulk magnetocrystalline anisotropy constant for magnetite, $K=1.2\text{x}10^5$ erg/cc, the critical diameter is 15nm. However, a more rigorous treatment of these two reversal mechanisms and their role in the theory of magnetic hyperthermia will be treated in chapter 3.

2.3 Stoner-Wohlfarth Model:

In section 2.1 and 2.2 it was noted that the particles in the ferrofluids used in this investigation are single domain and reverse by coherent reversal mechanisms. It is therefore appropriate to discuss the Stoner-Wohlfarth model. The Stoner-Wohlfarth model [24] describes the mechanism of magnetisation reversal by coherent rotation i.e. all moments within the particle remain parallel during their reversal. The model assumes single domain particles that reverse in isolation.

The model states that the energy barrier that needs to be overcome in order for magnetisation reversal is due to the anisotropy of the particles. The model postulates a particle that has the shape of a prolate spheroid, such that the anisotropy is due to the shape anisotropy of the particle. This is shown diagrammatically in figure 2.4, where c is the major axis, a is the minor axis, θ is the angle between the easy axis and the magnetisation vector and α is the angle between the easy axis and the applied field. It should be noted that the model is also valid for spherical particles with uniaxial magnetocrystalline anisotropy.

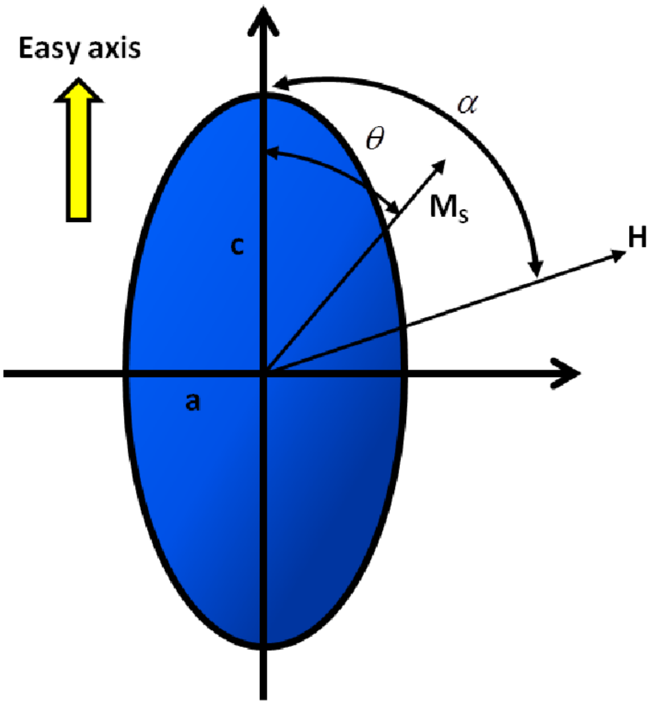

Figure 2.4: Schematic of the single domain prolate spheroid on which the Stoner-Wohlfarth theory is based.

In order to quantify the energy barrier involved with magnetisation reversal by coherent rotation, the energy contributions involved must be discussed. The anisotropy energy of a uniaxial single domain particle, like that given in figure 2.4, is given by equation 2.6.

$$E_A = KVsin^2\theta \tag{2.6}$$

If a field is applied to this particle at an angle α to the easy axis, then the material acquires a potential energy, given by equation 2.7.

$$E_H = -HM_SVcos(\alpha - \theta) \tag{2.7}$$

Where H is the external magnetic field and M_S is the saturation magnetisation. Thus, the total energy of the material is the sum of the anisotropy energy and the potential energy due to the field. This is shown by equation 2.8.

$$E = E_A + E_H = KVsin^2(\theta) - HM_SVcos(\alpha - \theta) \tag{2.8}$$

Taking the differential of the total energy in equation 2.8 with respect to the angle θ (the angle between the easy axis and the magnetisation vector) gives equation 2.9.

$$\frac{dE}{d\theta} = 2KVsin(\theta)cos(\theta) - HM_SVsin(\alpha - \theta) \tag{2.9}$$

It is trivial then to solve equation 2.9 for the minimum and maximum energy positions of the magnetisation vector. In the absence of an external field, the minimum energy occurs when the magnetisation vector is parallel to the easy axis. The maximum value then occurs when the magnetisation vector is perpendicular to the easy axis. The difference between the maximum and minimum energies gives the energy barrier of reversal for the particle. This is shown by equation 2.10 where H_K is the anisotropy field given by equation 2.11. Note that equation 2.11 is valid for the aligned case of uniaxial particles, for the case of random orientations the constant is reduced to 0.96.

$$\Delta E = KV\left[1 - \frac{H}{H_K}\right]^2 \tag{2.10}$$

$$H_K = \frac{2K}{M_S} \tag{2.11}$$

It should be noted that in the case of cubic anisotropy the energy barrier involved in moving from on easy direction another is reduced [25] [26]. Therefore, equation 2.10 is modified to equation 2.12, in the case of a positive anisotropy value.

$$\Delta E = \frac{KV}{4}\left[1 - \frac{H}{H_K}\right]^2 \tag{2.12}$$

Furthermore, the Stoner-Wohlfarth theory predicts the dependence of the magnetisation process on the angle between the applied field and the easy axis of the particle. This is achieved by combining the equation for the minimum energy (equation 2.9) and the component of the magnetisation vector in the direction of the applied field. This relationship is demonstrated by figure 2.5.

From figure 2.5 two important cases can be highlighted. Firstly, when the field is applied at 90° to the easy axis, the reduced magnetisation ($m=M/M_S$) is linear with respect to the applied field. The magnetisation saturates when the value of the applied field equals the value of the anisotropy field (equation 2.11). The magnetisation curve shows no hysteresis, remanence or coercivity. Secondly, when the field is applied parallel to the easy axis and the curve is characterised by a rectangular hysteresis loop where the magnetisation switches when the field applied equals the anisotropy field.

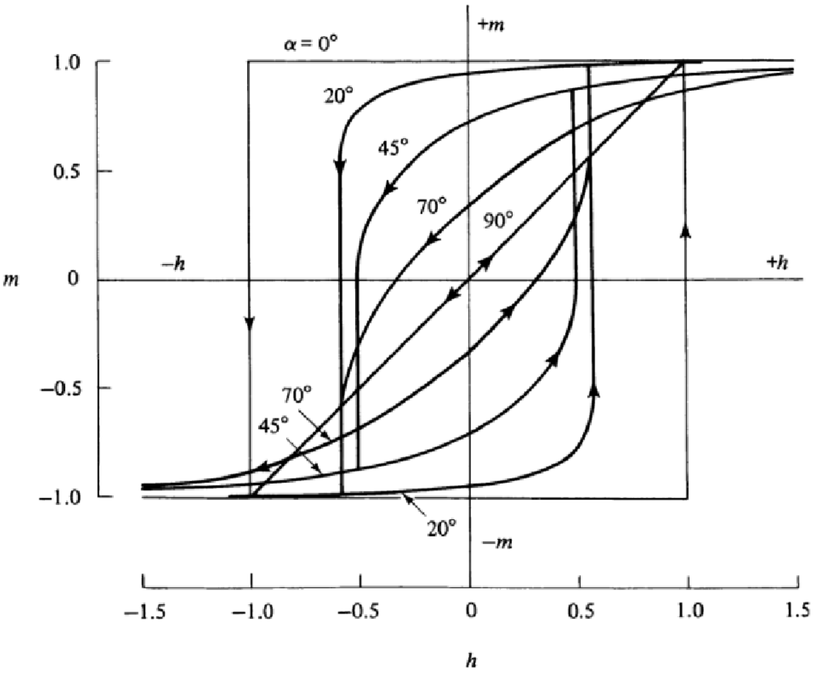

Figure 2.5: magnetisation curves as a function of applied field angle ([21] from [24]).

2.4 Thermal Activation of Magnetisation:

All physical systems exhibit fluctuations in their thermal energy on the microscopic scale. Néel [22] postulated that if the volume of a single domain particle became small enough then the thermal energy will be enough to overcome the anisotropy energy barrier and result in the magnetisation spontaneously reversing in zero field. This property is referred to as superparamagnetism [27].

The name superparamagnetism comes from the fact that these particle behave like classic paramagnets. This being that in the presence of an external field the particles will align themselves with the field. However, the thermal energy of the particle will attempt to break the alignment; this is shown by figure 2.6. In a classic paramagnet however, the moment involved is that of single atoms and ions. Whereas in a superparamagnetic material the moment is many thousands of times larger. Additionally, the full magnetisation curve, up to saturation, can be observed at normal fields and temperatures, unlike the very high fields and low temperatures needed for normal paramagnetic materials.

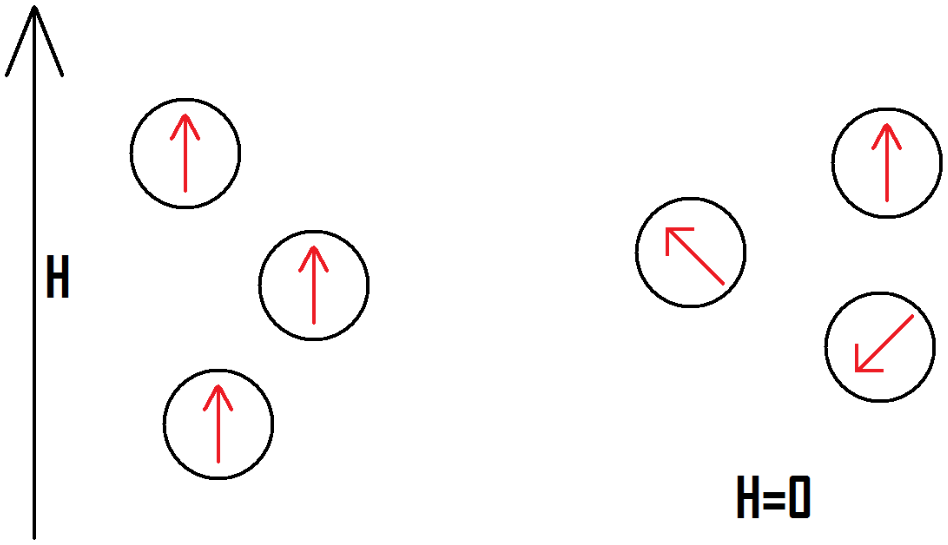

Figure 2.6: In the absence of an external field thermal fluctuation act to create randomly orientated magnetisation vectors.

Superparamagnetic magnetisation curves display two unique features. Firstly, there is no hysteresis i.e. no remanent magnetisation and a coercive field of zero. Secondly, curves measured at different temperatures will superimpose when the magnetisation is plotted as a function of field divided by temperature.

Superparamagnetism is a behaviour which depends on certain critical parameters. For a constant temperature there is a critical volume below which particles are superparamagnetic. In other words, particles that are small enough so that the thermal fluctuations are enough to overcome the energy barrier for reversal. Similarly, for particles of a constant volume there is a critical temperature above which the particles will be superparamagnetic. These parameters depend on the rate of relaxation of the magnetisation. When these critical parameter are not satisfied the superparamagnetic nature of the material will disappear and hysteresis will be observed.

Taking an assembly of particles magnetically saturated with a field parallel to their easy axes in some direction and then the field removed. Some of the particles in the assembly will immediately reverse their magnetisation because their thermal energy is greater than the average and magnetisation of the assembly will begin to decrease. The rate of the decrease of magnetisation at any time is proportional to the magnitude of the magnetisation existing at that time. This means that the magnetisation is proportional to the Boltzmann factor (exp(-KV/K_BT)) because this factor represents the probability that a particle has enough thermal energy to overcome the energy barrier for reversal.

There is a relaxation time τ, associated with superparamagnetism and is defined as the time taken for the remanent magnetisation to be reduced by 1/e. For a system with uniaxial anisotropy in zero field the relaxation time is given by equation 2.13. The scope of the relaxation time can be seen in figure 2.7.

$$\frac{1}{\tau} = f_0 exp\left[-\frac{KV}{K_B T}\right] \tag{2.13}$$

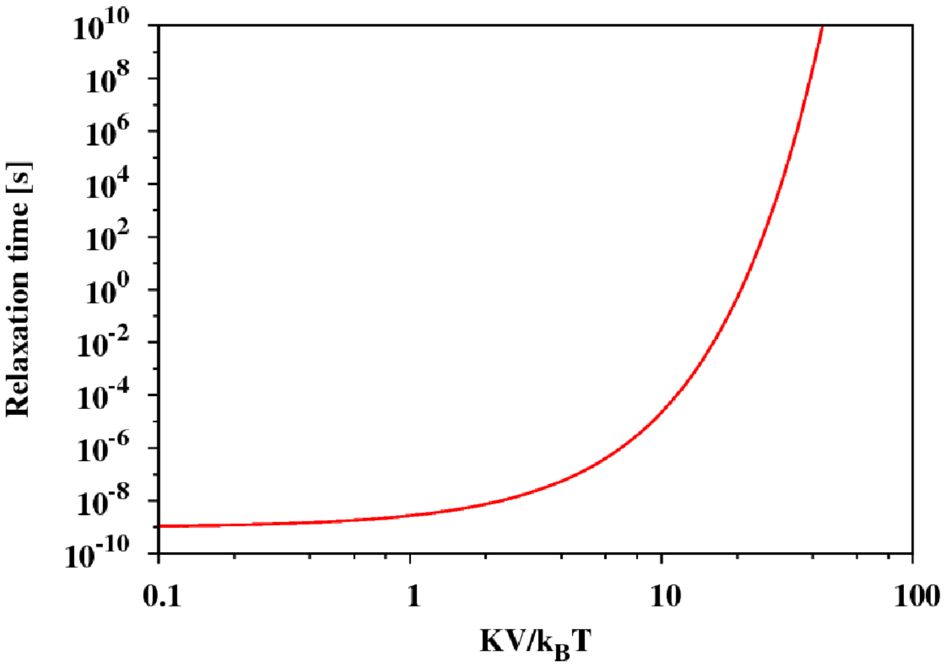

Figure 2.7: Plot showing the range of relaxation times for constant K and T and a variation in volume.

A system is defined as being superparamagnetic if the relaxation time is less than the time it takes to make a measurement of the system's remanence. This time is generally taken as being 100 seconds. Assuming this value of the relaxation time and the previously mentioned value of f_0 then equation 2.13 can be solved for the critical volume and the critical temperature, these are shown by equation 2.14 and equation 2.15 respectively.

$$V_P = \frac{25 K_B T}{K} \tag{2.14}$$

$$T_B = \frac{KV}{25 K_B} \tag{2.15}$$

By inspection it can be seen that the transition to stable behaviour occurs when the energy barrier becomes equal to 25K_BT (for uniaxial particles). For particles of a constant size, the critical temperature, below which the magnetisation is stable, is referred to as the blocking temperature, T_B.

Since these two critical parameters depend on the energy barrier, these values are different for multiaxial anisotropy. The modified critical volume and blocking temperature are given by equations 2.16 and 2.17 respectively, for a system with cubic anisotropy and a positive anisotropy value.

$$V_P = \frac{100K_BT}{K} \tag{2.16}$$

$$T_B = \frac{KV}{100K_B} \tag{2.17}$$

Thus far superparamagnetism in the absence of an applied field has been discussed. However, earlier (section 2.3) it was shown that the energy barrier is reduced in the presence of an applied field (equation 2.10). Therefore, particles larger than the critical size, which would be stable in zero field and would not thermally reverse in 100 seconds, can overcome the energy barrier. This is the case when the energy barrier is lowered to 25K_BT. This is shown by equation 2.18. Here the field is the coercive field, H_C.

$$\Delta E = KV\left[1 - \frac{H_CM_S}{2K}\right]^2 = 25K_BT \tag{2.18}$$

2.5 Frequency Dependence of Hysteresis:

Magnetic hyperthermia employs the use of an alternating magnetic field. Time dependencies of the magnetisation mean that there is a frequency dependence of the magnetic hysteresis observed within the system. By making the simple assumptions that the particles within a system are non-interacting and that the external field is applied parallel to the easy axes of these particle, the Sharrock law [28] give the time dependent value of the coercive field. This is shown by equation 2.19.

$$H_C(t) = H_K\left[1 - \sqrt{\frac{K_BT}{KV}\ln\left(\frac{tf_0}{0.693}\right)}\right] \tag{2.19}$$

In the case of an alternating magnetic field the parameter t in equation 2.19 becomes an effective time t_{eff}. This effective time is dependent on the sweep rate of the field [29]. The effective time is given by equation 2.20.

$$t_{eff} = \frac{K_B T R^{-1} H_K}{2KV\left(1-\frac{H_C}{H_K}\right)} \tag{2.20}$$

Where R is the sweep rate of the field. Substituting equation 2.20 into equation 2.19 results in equation 2.21. Equation 2.21 [30] gives the value of the coercive field and consequently the hysteresis as a function of the sweep rate.

$$H_C(R) = H_K\left[1 - \sqrt{\frac{K_B T}{KV}\ln\left(\frac{K_B T f_0 H_K}{2KVR(1-h_C)}\right)}\right] \tag{2.21}$$

Where h_C is the reduced coercive field ($h_C=H_C/H_K$).

At high sweep rates there is an increase to both the remanence and coercivity observed. This also increases the squareness of the hysteresis loop. This can be seen in figure 2.8 [31].

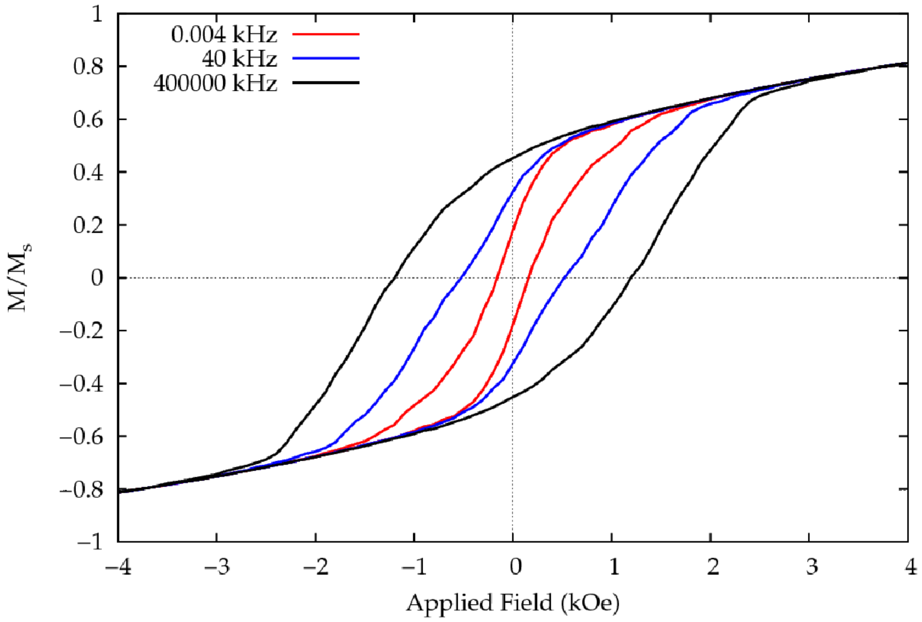

Figure 2.8: Plot showing the increase of magnetic hysteresis at high field frequencies [31].

This is important for magnetic hyperthermia as the heat released by hysteresis loss (see section 3.3) is proportional to the square of the frequency. Physically, at higher sweep rates of the applied field a greater fraction of the larger superparamagnetic particles have a relaxation time longer than the time needed for a complete sweep of the loop. The hysteresis loops for these frequencies are wider because more particles contribute to the hysteresis losses by exhibiting thermally stable behaviour. This is supported by the fact that in a real system there will be a distribution of particle sizes and therefore a distribution of particles that are observed to be superparamagnetic.

For medical applications of magnetic hyperthermia there is a restriction on the frequency values of the alternating field. For clinical applications of magnetic hyperthermia physiological considerations need to be taken. At higher frequency magnetic fields, local heating in non-magnetic tissues may be caused by induced eddy currents. The Brezovich limit [32] gives a limiting value for the product of the magnetic field amplitude and frequency: $Hf < 3.86\text{x}10^{10}$ Oe/s ($4.85\text{x}10^{8}$ A/m s). Below this limit the alternating field does not cause excessive heating in patients. Technical considerations have limited the frequencies used thus far in medical studies of hyperthermia in biological tissue to a narrow range, from 100 to 150 kHz [33].

2.6 Energy Barrier Distribution:

So far in this section the role of magnetisation reversal and its mechanisms have been discussed. Throughout, the concept of an energy barrier has been highlighted. The energy barrier is the key parameter that prevents the magnetisation reversal; this can be due to an external field or thermal fluctuations. In the presence of an external field of any magnitude and at any temperature, the value of the magnetisation is dependent upon the number of particles within the system that have crossed the energy barrier and have been allowed to align with the field.

Thus far the energy barrier has been discussed in the context of specific situations. However, in real systems, which have a distribution of parameters such as size, shape and anisotropy, there will be a distribution of energy barriers. A real system will have an energy barrier distribution similar to that shown in figure 2.9.

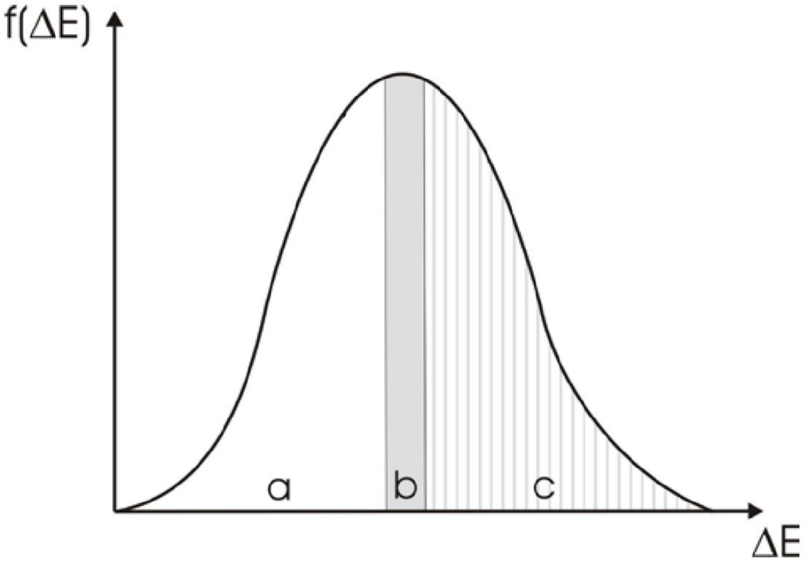

Figure 2.9: Energy barrier distribution.

In figure 2.9, the energy barrier distribution shows the number of particles in the system having a particular value of the energy barrier. Considering a system with a distribution of energy barriers which is saturated in a positive external field and then the field reversed in direction (not necessarily to saturation). For the majority of particles the energy barrier is that needed in order to overcome the anisotropy forces. This corresponds to region b of figure 2.9. A lower fraction of the particles in the system, usually the particles of a smaller volume, will be superparamagnetic in nature and will spontaneously rotate to the negative direction via thermal fluctuations in the time of the measurement. This corresponds to region a of figure 2.9. For the remaining particles, usually having a larger volume, the magnetisation remains pointed in the original direction because they cannot reverse in the time of measurement for the given field. This corresponds to region c of figure 2.9. It should be noted that in the case where the initial saturating field is not applied parallel to the easy axis, the magnetisation aligns with the field out of an easy axis. When the field is remove the magnetisation will spontaneously rotate to the closest easy direct, this results in a partial lowering of the energy barrier.

The energy barrier distribution can be determined from measurements of the susceptibility or from measurements of the remanent magnetisation. In this work the energy barrier is determined via the remanent magnetisation. The advantage of this method is that the energy barrier in zero field is simply KV (for the uniaxial case) and knowledge of the anisotropy field is not required. For a system of randomly aligned particles the remanent magnetisation is give by equation 2.22.

$$\frac{M_R}{M_S}(T) = \frac{M_R}{M_S}(0)\left[1 - \int_0^{V_P} f(V)dV\right] \tag{2.22}$$

Where M_R is the remanent magnetisation and f(V) is the volume distribution of the system. From equation 2.22 there a link between the energy distribution and the particle size distribution.

Experimentally, the energy barrier distribution can be directly obtained from the differential of a temperature decay of remanence curve. Due to the fact that these measurements are carried out in zero field, care must be taken to account for the effects of the demagnetising field. These can be minimised using elongated samples and dilute systems, hence ferrofluids are well suited to this type of measurement.

Chapter 3: Magnetic Hyperthermia

In this chapter a model of magnetic hyperthermia is outlined. The direction of the work in this thesis is dictated by the theoretical and experimental studies conducted by the magnetic materials research group at The University of York presented in [34] and [35].

The chapter begins by outlining the mechanisms by which heat is generated during magnetic hyperthermia. These methods are then expanded upon with regard to the size of their contribution and the critical limits that apply. The chapter then moves on to describe the effects of distributed systems on the heat generated.

3.1 Heating Mechanisms:

The heat dissipated by magnetic nanoparticles in an oscillating magnetic field is produced by multiple physical processes. The exact mechanisms for the heat generation and their relative contributions have been the subject of research for many years. In the model of magnetic hyperthermia described by G. Vallejo-Fernandez, et al [34], three major heating mechanisms are suggested. These are the mechanisms associated with susceptibility loss, hysteresis loss and viscous heating (magnetic stirring).

Susceptibility loss occurs in superparamagnetic particles. Since there is a critical size for superparamagnetic behaviour, there is a critical limit for heating via susceptibility losses. The critical diameter for susceptibility loss is given by equation 3.1 [27].

$$D_P(0) = \left(\frac{6K_BT\ln(tf_0)}{\pi K}\right)^{\frac{1}{3}} \tag{3.1}$$

Where T is the temperature. Below this critical diameter particles will contribute to susceptibility loss. Above this diameter particles will be blocked and the particles will not generate heat via susceptibility loss.

Above the critical value $D_P(0)$ the particles will switch in the alternating field and heating due to hysteresis loss will occur. The critical size given by equation 3.1 is the critical size for zero or small field. For magnetic hyperthermia studies fields of approximately 200 Oe and frequencies of about 100 kHz are used [36]. The small amplitude of the field will limit the fraction of the blocked particles that can undergo reversal in the alternating field. The fraction of particles that can switch is also size dependent. This results in a critical upper limit for hysteresis heating. Above this upper limiting diameter, given by equation 3.2, particles will not switch in the field and will not contribute to hysteresis heating or susceptibility loss. Note that the constant (0.96) in equation 3.2 is due to the random orientation of easy axes in a ferrofluid. This is such that the anisotropy field is given as H_K=0.96K/M_S [38]. The consequence of these two critical sizes is that only particles of diameter $D_P(0)<D<D_P(H)$ contribute to hysteresis heating.

$$D_P(H) = \left[1 - \frac{HM_S}{0.96K}\right]^{-\frac{2}{3}} D_P(0) \tag{3.2}$$

For particles larger than the critical size $D_P(H)$ the moments cannot switch in the low amplitude field. However, the majority of these particles are not aligned with the axis of the applied field and viscous heating due to stirring of the particles will occur. This stirring adds heat to the system and is the final mechanism for heat generation in hyperthermia. The limiting values for the heating mechanisms with regard to the size distribution of particles are shown by figure 3.1.

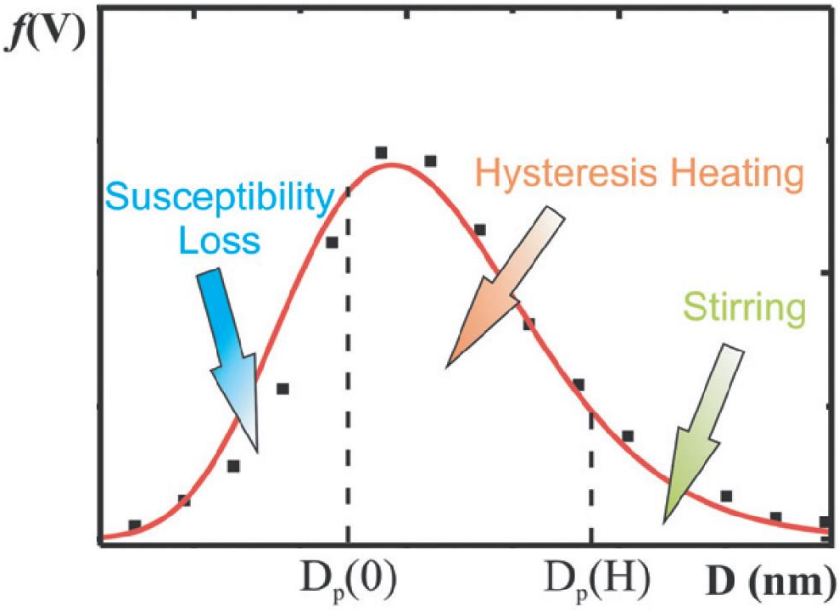

Figure 3.1: A typical particle size distribution showing the critical limits for hysteresis heating.

3.2 Magnetic Susceptibility Heating:

Magnetic susceptibility heating occurs in superparamagnetic particles and is a combination of Néel relaxation and Brownian rotation due to the particles existing in a liquid environment (see section 2.2.2). The combination of these two processes leads to a combined relation time τ_{Tot}, for susceptibility loss [37], give by equation 3.3.

$$\tau_{Tot} = \frac{\tau_N \tau_B}{\tau_N + \tau_B} \tag{3.3}$$

The terms in equation 3.3 are the relaxation times associated with Néel and Brownian relaxation from equations 2.3 and 2.4 respectively. Susceptibility heating does not apply above the limit for superparamagnetic behaviour $D_P(0)$.

The heat generated by susceptibility loss can be quantified as the power generated via susceptibility loss and is given by equation 3.4 [37].

$$P_{ac} = \pi f \chi'' H^2 \tag{3.4}$$

Where f is the frequency of measurement (f=1/t), χ'' is the complex part of the ac susceptibility and is given by equation 3.5.

$$\frac{\chi''}{\chi_0} = \frac{2\pi f \tau_{Tot}}{1+2\pi f \tau_{Tot}{}^2} \tag{3.5}$$

Where χ_0 is the initial dc susceptibility. The mechanisms of Néel relaxation and Brownian rotation are shown in figure 3.2.

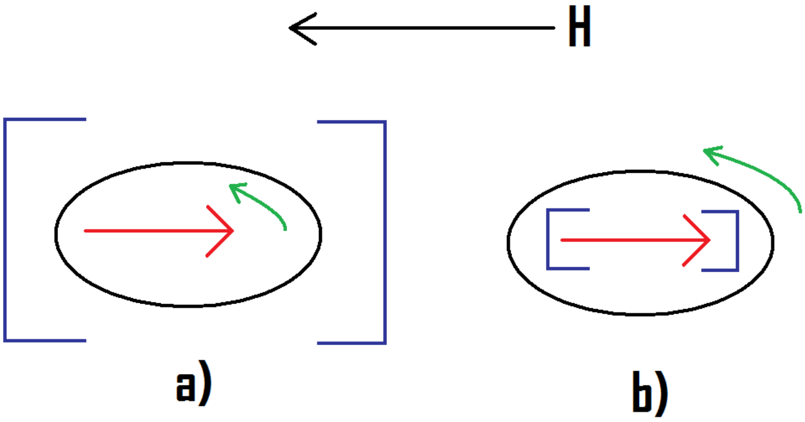

Figure 3.2: A superparamagnetic particle rotating by a) Néel relaxation and b) Brownian rotation.

It has been shown previously by G. Vallejo-Fernandez, et al [34] that the main contribution to the susceptibility loss at 100 kHz (frequency commonly used in studies of hyperthermia) is due to Brownian rotation. The volume dependence of the relaxation times means that there is a transition from Néel to Brownian reversal and at a frequency of 100 kHz the Néel contribution is negligible. Brownian rotation is a dynamic effect that dependent upon the viscosity of the liquid environment. For medical applications of magnetic hyperthermia it is believed that the in vivo viscosity is significantly higher than in the pure colloid and such dynamic effects will largely be suppressed. For example, the viscosity of blood is ~10cP. The conclusion is that for magnetic hyperthermia the heating contribution due to magnetic susceptibility heating can be neglected.

3.3 Hysteresis Heating:

For particles above the superparamagnetic limit $D_P(0)$ the particles will be blocked and will switch in the alternating field. In this case the heat is due to hysteresis energy loss. As stated previously, in medical hyperthermia fields of approximately 200 Oe are used. For this value of the field, only a fraction of the particles will be able to reverse in the time taken to sweep the field once. This means that particles above the critical size $D_P(H)$ will not contribute to hysteresis heating. The two limiting diameters restrict hysteresis heating to particles with diameter $D_P(0)<D<D_P(H)$.

The amount of heat generated is proportional to the frequency multiplied by the area of the hysteresis loop. However, it is only the irreversible part of the magnetisation that contributes to this effect. Since particles in a ferrofluid are randomly orientated, their remanence is theoretically $0.5M_S$. The power generated by hysteresis heating is given by equation 3.6.

$$P_{hys} = \frac{2M_S f}{\rho} \int_{D_P(0)}^{D_P(H)} H_C(D) f(D) dD \tag{3.6}$$

Where ρ is the density of the magnetic material, f(D) is the particle size distribution and $H_C(D)$ is the size dependent coercive field (switching field) given by equation 3.7.

$$H_C(D) = H_K \left[1 - \left(\frac{6 \ln(t f_0) K_B T}{\pi K D^3}\right)^{\frac{1}{2}}\right] \tag{3.7}$$

The power generated by hysteresis heating is dependent on the value of the anisotropy of the particles. In most models of hyperthermia this value is assumed to be a constant. However, in a real system there is likely to be a distribution of anisotropy constants. Physically, the effect of a distribution of anisotropy constants would be to broaden the overall energy barrier distribution. As discussed in section 2.6, this would lower the fraction of particles that would switch in the field. In other words, predictions of the heating caused by hysteresis loss would be overestimated if the value of the anisotropy is taken to be constant. For the purpose of clinical applications, in order to produce a desired amount of heating by hysteresis loss, control over the anisotropy dispersion is required. This is in addition to control over the particle size distribution.

For magnetite nanoparticles, anisotropy is composed of two components: the magnetocrystalline anisotropy and the shape anisotropy. The shape anisotropy is given by equation 3.8.

$$K_S = \frac{1}{2}(N_a - N_c)M_S^2 \tag{3.8}$$

Where N_a and N_C are the shape demagnetising factors for a prolate spheroid and are given by equations 3.9 and 3.10. Where r is the aspect ratio (r=c/a).

$$N_c = \frac{4\pi}{r^2-1}\left[\frac{r}{\sqrt{r^2-1}}\ln\left(r+\sqrt{r^2-1}\right)-1\right] \tag{3.9}$$

$$N_a = \frac{4\pi - N_c}{2} \tag{3.10}$$

Figure 3.3 shows the variation of shape anisotropy with aspect ratio. The value of the magnetocrystalline anisotropy (elongation independent) for magnetite is shown. The value of K_C for a magnetite ferrofluid is one quarter of the bulk anisotropy constant (discussed in section 2.3). The shape anisotropy variation was calculated using M_S=400 emu/cc (typical for magnetite). Figure 3.3 demonstrates that for particles with aspect ratios greater than 1.05, the shape anisotropy dominates over the magnetocrystalline anisotropy, K_C. For particles with aspect ratios between 1.0 and 2.0 the value of the shape anisotropy can change dramatically. Since the size of the particles used in clinical hyperthermia exhibit elongations in this range, the shape anisotropy distribution must be significant.

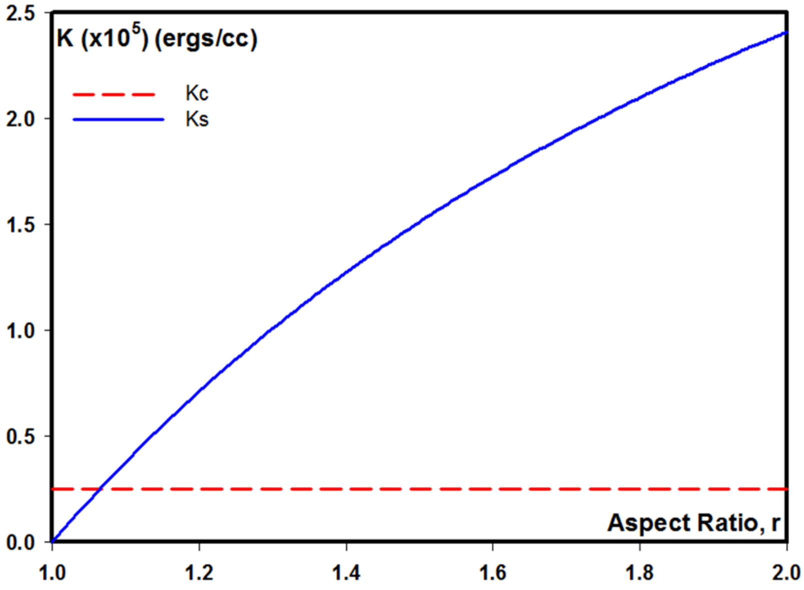

Figure 3.3: Plot of the shape anisotropy variation with aspect ratio.

3.4 Magnetic Stirring Effects:

Particles above the critical size $D_P(H)$ do not reverse in the small fields used for clinical magnetic hyperthermia and so do not contribute to magnetic hysteresis heating. Since nanoparticles in a ferrofluid are orientated randomly, most will not be aligned with the axis of the solenoidal field and viscous heating due to stirring of the particles in the colloid will occur. This drag force will add heat to the system. At a frequency of 100 kHz this effect will be significant, especially when aggregates of particles are present. Due to the lack of control over the amount of aggregation in ferrofluids, the anomalously large heating effects that have previously been reported [39] can be explained. Over time the particles will align themselves with the field axis, this explains the non-linear heating rates that have been reported in the literature [40]. The stirring effect can be shown diagrammatically in figure 3.4.

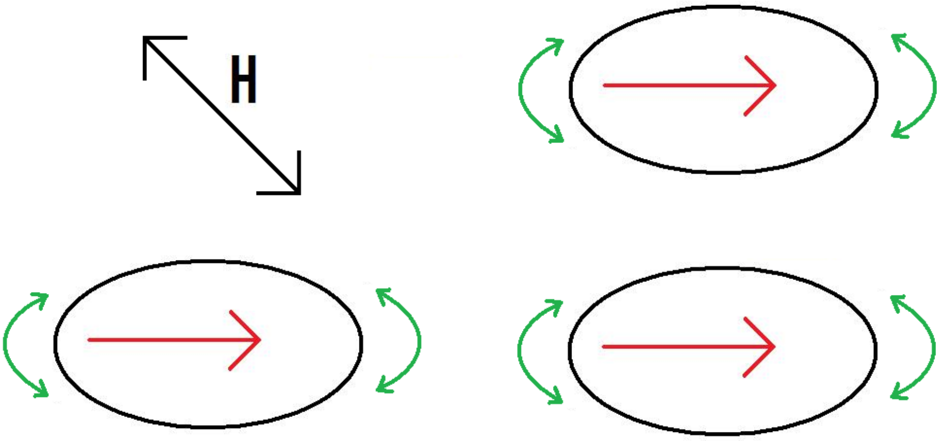

Figure 3.4: Nanoparticles trying to align with the solenoidal field. This causes drag in the liquid environment.

Calculations for the power generated by magnetic stirring are extremely complex. The frictional drag between the particles and the liquid is unknown and at 100 kHz the flow of the liquid about the oscillating particles will be turbulent and cannot be predicted by classical hydrodynamics. The heat generated by the stirring is impossible to control. Fortunately for clinical application of magnetic hyperthermia, the in vivo environment has a higher viscosity than in the pure colloid. Since the amount of heat generated by magnetic stirring will decrease with increasing viscosity, the heat generated by magnetic stirring is negligible in vivo and can be discounted for medical applications.

3.5 Effect of Distributed Systems:

3.5.1 Effect of Particle Size Distribution:

For fine particle systems the distribution of particle sizes generally takes the form of a lognormal distribution [41] given generally by equation 3.11.

$$f(y)dy = \frac{1}{\sqrt{2\pi}\sigma y} exp\left[-\frac{\left(\ln\left(\frac{y}{y_m}\right)\right)^2}{2\sigma^2}\right]dy \qquad (3.11)$$

Where y is some variable, y_m is the median value of the variable from the distribution and σ is the standard deviation of ln(y). Since the particle diameter is lognormal the volume distribution is also lognormal.

The standard deviation of the distribution, σ gives important information about the width of the distribution. G. Vallejo-Fernandez and K. O'Grady [35] investigated the effect of the standard deviation of the particle size distribution on hysteresis heating. This is demonstrated by figure 3.5 [35], which shows how the heat output varies when the standard deviation in particles size, σ_D, changes while the median diameter remains D_m remains constant. This is shown for two different values of D_m and different values of the standard deviation of the anisotropy distribution, σ_K, are given.

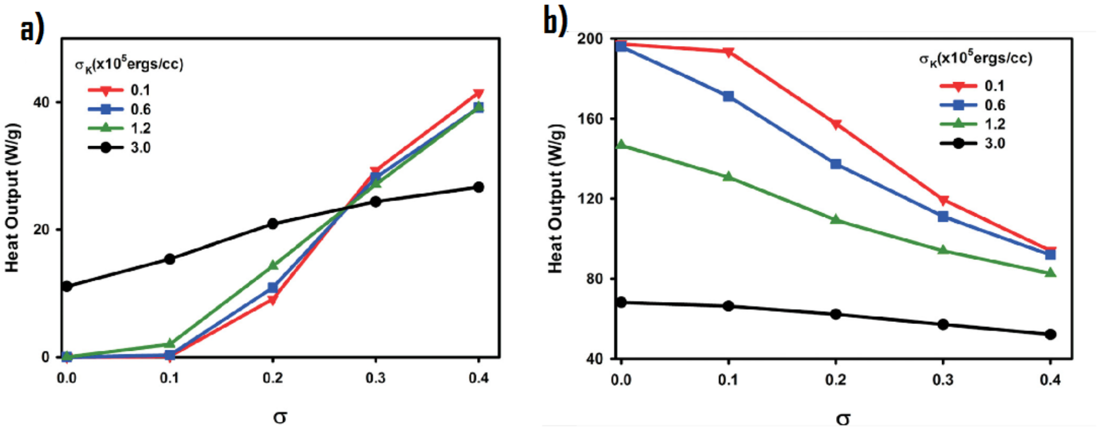

Figure 3.5: Heat output as a function of the standard deviation of particle sizes for different values of σ_K for particles of median size a) 10.3 nm and b) 15.2 nm [35].

Figure 3.5a shows that the heat generated increases as the width of the particle size distribution increases. This is because a greater fraction of the particles are blocked. However, in the case of larger particles (figure 3.5b) the opposite effect is observed because the distribution is shifted such that a greater fraction of the particles have a diameter larger than $D_P(H)$. Therefore, fewer particles contribute to hysteresis heating. It can be seen from figure

3.5 as a whole that the width of the anisotropy distribution can have the effect of increasing or decreasing the heat generated by hysteresis loss. Therefore, It is necessary to consider both the particle size distribution and the anisotropy distribution [35].

3.5.2 Effect of Anisotropy Distribution:

The effect of the anisotropy distribution has been considered in [35] by assuming a lognormal distribution of shape anisotropy constants. Figure 3.6 shows the variation in the heat output for particles of different sizes as a function of σ_K (related to the width of the anisotropy distribution). The median value of the anisotropy K_m is constant in figure 3.6 and is applicable to particles with elongations discussed in section 3.3.

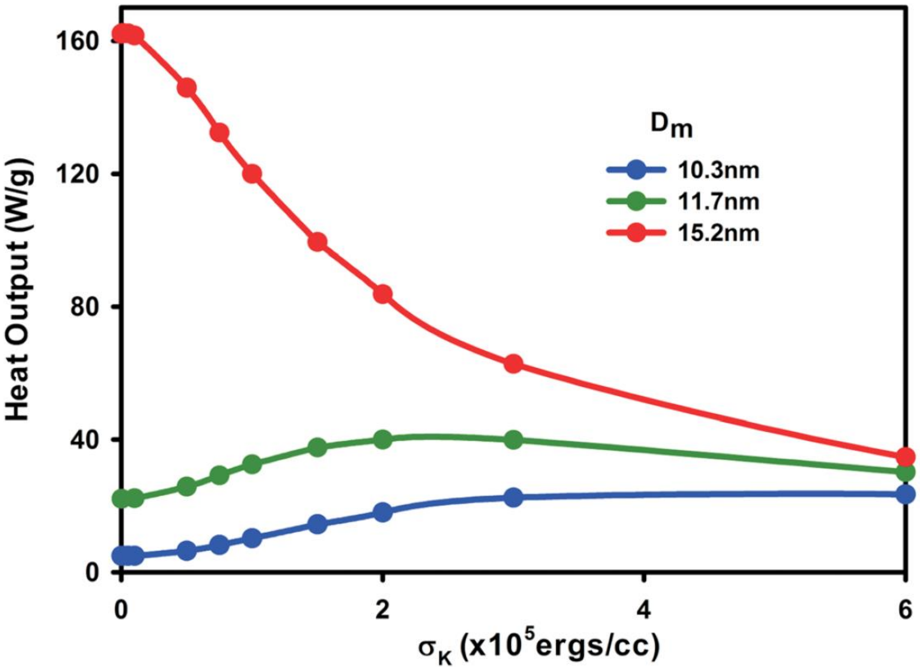

Figure 3.6: Heat output as a function of the standard deviation in the anisotropy constants for particles of different median sizes [35].

From figure 3.6 it can be seen that in the case of smaller particles and narrow anisotropy distributions the amount of heat generated increases with σ_K. This is due to the fact that more particles in the distribution become blocked. However, as σ_K increases further, an even greater fraction of the particles will have switching fields (equation 3.7) that are greater than the field amplitude used in hyperthermia. These will no longer contribute to the heating. This is shown by the levelling off of the curves in figure 3.6. For larger particles, the heat generated decreases with σ_K. This is because most of the particles in the system are already blocked and a broader distribution will result in a greater fraction of the particles having size above $D_P(H)$.

Inclusion of the anisotropy distribution adds complexity to the calculation for the power generated via hysteresis heating. Since the critical sizes $D_P(0)$ and $D_P(H)$ both rely on the anisotropy, these critical limits must then be modified to include a distribution of anisotropy constants. Additionally, the power generated by hysteresis heating given by equation 3.6 is therefore modified to equation 3.12 to take into account distributed anisotropy.

$$P_{hys} = \frac{2M_S f}{\rho} \int_0^\infty \int_{D_P(0,g(K))}^{D_P(H,g(K))} H_C(D) f(D) g(K) dDdK \tag{3.12}$$

Where g(K) is the lognormal distribution of the shape anisotropy constants.

In summary, it has been shown that of the original three mechanisms, hysteresis heating is the dominant mechanism of heat generation. The anisotropy affects the critical parameters that determine the fraction of particles that contribute to hysteresis heating as well as the amount of heat generated. Therefore, an understanding of the distribution of anisotropy constants is of paramount importance for an accurate model of magnetic hyperthermia and is critical for clinical uses of magnetic hyperthermia.

Chapter 4: Experimental Techniques

In this chapter the apparatus and measurement techniques used to characterise the physical and magnetic properties of the samples used in this investigation are described. An overview of the type of samples and their growth is presented.

The experimental techniques associated with the physical characterisation are addressed first. The basic principles of transmission electron microscopy and X-ray diffraction are outlined in the context of the experiments performed herein. The procedures for measuring both the size and shape distributions are explained in detail. These procedures allow the shape anisotropy distribution of any sample to be determined.

The magnetic characterisation is addressed next. The motivation and methodology of the temperature decay of remanence measurement are summarised. The chapter concludes with details of the heating measurements performed and the apparatus used.

4.1 Sample Preparation

All of the ferrofluid samples used in this work were supplied by Liquids Research Limited [42]. The precise method of their chemical growth is confidential. However, the method is based on that patented by Khalafalla and Reimers [43]. A brief explanation is given here for the benefit of the reader.

The quality of a ferrofluid is determined by two characteristics. Firstly, the size and size distribution of the nanoparticles in the fluid must be controlled. Secondly, the surfactant coating must provide enough particle separation for the fluid to suit its purpose. The process cited above improves upon the original grinding method of ferrofluid production, in which a ferrimagnetic material is milled down to nanometre size.

This method was later refined into the current co-precipitation method in which a stoichiometric aqueous solution of ferrous and ferric compounds is prepared. Through controlled reaction parameters ferrous and ferric ions are precipitated from the solution and magnetic nanoparticles are grown in situ. Following the initial precipitation the particles undergo a controlled growth process (CGP). Once grown, surfactants and carrier solutions can be added in turn. The result is a stable ferrofluid containing nanoparticles like those shown in figure 4.1.

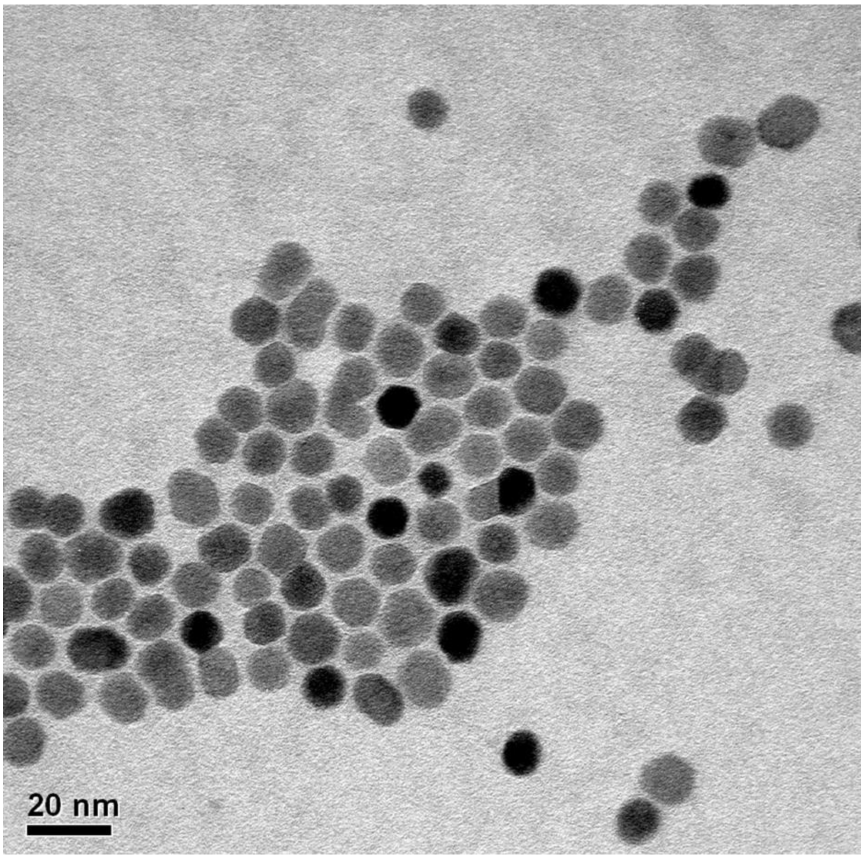

Figure 4.1: Magnetite nanoparticles grown via the controlled growth process [35].

4.2 Structural Analysis:

In order to characterise the physical properties of nanoparticles two observations must be made. Firstly, the nanoparticles themselves must be imaged in order for size and shape distributions to be deduced. This can be done using transmission electron microscopy (TEM). The second observation is that of the crystal structure of the nanoparticles. This analysis can be achieved using X-ray diffractometry.

4.2.1 Transmission Electron Microscopy:

All nanoparticle shape and size distribution measurements in this work are based on TEM images. The transmission electron microscope was first proposed by Knoll and Ruska [44], [45]. Electrons, whose wavelength is less than that of visible light, can be used to resolve objects far smaller than those observed using conventional microscopes. The TEM does this using a series of magnetic lenses and electron opaque apertures. The TEM used in this work was a JEOL 2011 TEM [46].

Figure 4.2 shows a schematic diagram of a standard TEM vacuum column, showing the major apertures and lenses. Note that the final image in figure 4.2 refers to a bright field image. A beam of electrons is produced by a filament (tungsten or LaB_6) which is held at a bias voltage with a Wehnelt cap and an anode [47]. This electron source acts as a point source and condenser lenses are used to converge the beam. The configuration and strength of these lenses determines the spot sizes available. The condenser aperture is then used to remove the electrons that are scattered at high angles. The beam is then incident on the sample. The sample is mounted in a holder attached to a goniometer. This allows movement in x, y and z directions as well as a single axis of rotation. Electrons transmitted through the sample are dispersed by an objective lens, creating a diffraction pattern. This pattern is combined by an intermediate lens and projected onto a phosphorescent screen by a projector lens. Electrons scattered to high angles by the objective lens can be removed by the objective aperture. Use of the objective aperture increases the contrast of the projected image. The screen can be raised to allow the image to be projected onto a CCD camera. This description is by no means a complete description of the TEM but includes the main features needed to create bright field images on which the analysis herein is based.

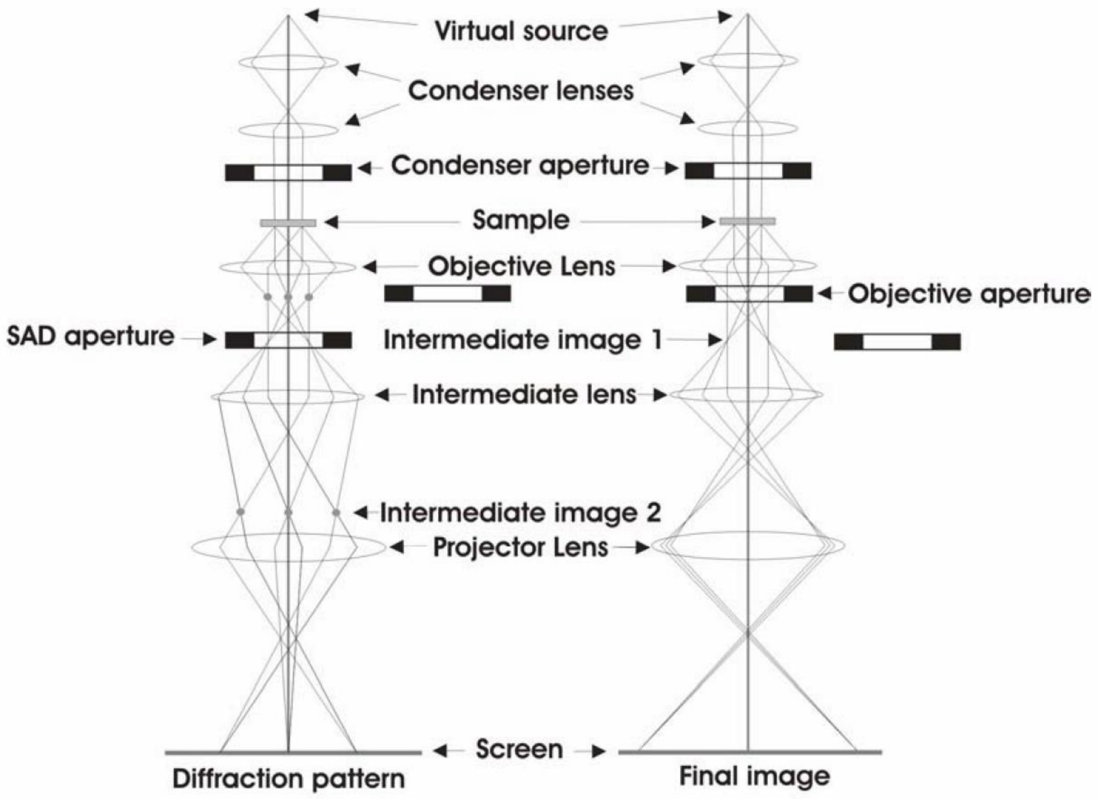

Figure 4.2: Schematic of a transmission electron microscope.

4.2.2 Composition analysis- X-ray diffraction:

In order to characterise the ferrofluid samples fully the material composition must be investigated. Ideally the magnetic response of the ferrofluids used in this work should come from magnetite (Fe_3O_4) nanoparticles. However, a real ferrofluid will contain other metal oxides, mainly maghemite (Fe_2O_3). Maghemite is formed via the oxidation of magnetite and can be thought of as a Fe^{2+} deficient magnetite. They both have the same spinel ferrite structure and both are biocompatible. As a result of these two features the presence of maghemite in the ferrofluids does not affect their viability for hyperthermia applications. Maghemite can be introduced into the chemical system via oxidation during various stages of the growth process or in situ depending on the characteristics of the colloid. The difference in the iron ions present will affect the magnetic response of the nanoparticles; specifically the coercivity, saturation magnetisation and the magnetocrystalline anisotropy. It is important to be able to determine the relative proportions of magnetite and maghemite. This can be done using X-ray diffraction.

Diffraction of electromagnetic radiation occurs in crystalline solids only when the wavelength of the radiation is comparable to the inter-atomic spacing. This wavelength resides in the X-ray region. X-ray diffraction is based on Bragg's law of diffraction. The law states that when radiation is incident on a crystalline solid, the constituent atoms absorb and re-radiate EM waves of the same (to a first order approximation) wavelength. Waves scattered by different atomic planes can interfere with each other constructively and destructively. Constructive interference occurs when the path difference between the two waves is equal to $2d\sin\theta$. Since there is an angular dependence for constructive interference, a diffraction pattern can be observed. Due to the complex nature of most solids, there are a large number of diffracting planes which produce a diffraction pattern consisting of mostly destructive interference and instances of high intensity constructive interference. Bragg's law is given by equation 4.1.

$$n\lambda = 2d\sin\theta_{Scat} \tag{4.1}$$

Where n is the diffraction order and takes an integer value, λ is the wavelength of the incident radiation, d is the spacing between atomic lattice planes and θ_{Scat} is the angle of scatter measured from the crystal plane.

The apparatus used in this work is a Rigaku SmartLab X-ray diffractometer [48]. The diffractometer consists of a motorised optical bench divided into three parts that move independently of each other. These parts, shown in figure 4.3, are the sample stage or goniometer, the X-ray source and the detector assembly. The goniometer simply holds the specimen and is able to move and rotate depending on the scan type.

The X-ray source used is a rotating copper-anode tube. Electrons are ejected from a tungsten filament and drawn towards a copper anode. Electrons are stopped by the copper target and produce a continuum of Bremsstrahlung radiation in addition to a characteristic line spectrum from electronic transitions in the copper. The complete X-ray spectrum produced is a superposition of the two and is dependent on the accelerating voltage; in this case the tube was held at a voltage of 45 kV and a current of 200 mA. The copper anode is a good choice for the anode as the copper K_α line is useful for most interplanar spacings [49]. Furthermore, the high thermal conductivity of copper means that it can be cooled easily and the rotation of the anode helps to spread the heat. The rest of the source assembly is comprised of slits to focus the X-rays and a filter to remove the copper K_β contribution to the X-ray spectrum.

The detector assembly consists of a number of receiving slits and the detector itself. The detector used in this diffractometer is a scintillator detector. A scintillator is a crystal, usually sodium iodide [50], which fluoresces when impacted by X-rays. The fluorescence is visible light whose intensity is proportional to the incident X-ray intensity. The scintillator crystal is connected to a photomultiplier tube (PMT), which amplifies and detects the fluorescence. The photons emitted by the scintillator release an electron from a photocathode in the PMT which is drawn to a number of dynodes along the tube, which create a cascade of electrons. This creates a pulse in the anode that is large enough to be detected. The speed of this process allows the detector to detect a large number of counts without significant signal loss due to lag.

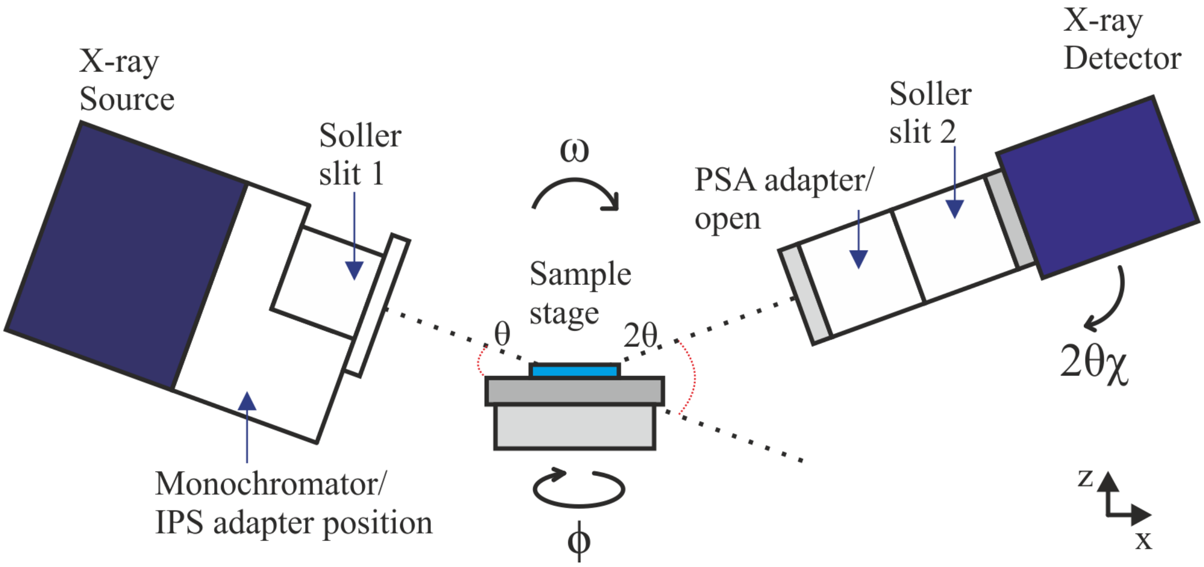

Figure 4.3: Fundamental set-up of an X-ray diffractometer. This shows the X-ray source, detector and sample stage.

The scan mode used in this work is a basic theta/2-theta scan. In this mode the sample is held still while the source and detector move in unison; such that they both keep the same angle θ_{Scat}, relative to the sample (see figure 4.3). This allows for the intensity of the diffracted X-rays to be measured as a function of the angle 2 θ_{Scat}. It should be noted that in figure 4.3 the source and detector assemblies move in the x-z plane only.

4.3 Particle Size Analysis:

The most useful method to characterise a ferrofluid sample is by its particle size distribution. Due to the irregular shapes of the nanoparticles a circular approximation is used for the size distribution. It can be shown that a sample of nanoparticles can be characterised by shape and this will be discussed in section 4.4. There is however a coupling between the shape and size of the particles. For a given elongation a particle can have a range of volumes. The exact nature of this coupling is not fully understood and it is not always useful to differentiate between two samples using the shape distribution.

The size distribution is measured using a Zeiss particle size analyser. A bright field TEM image is printed and placed on the front of a light box. An iris projects a circular beam of light onto the TEM image which can be seen through the paper. The diameter of the iris can be adjusted to change the size of the light beam. To measure a particle the iris is adjusted such that the circular beam has an area equivalent to that of the particle. When a foot pedal is depressed a computer records the current size of the iris and a mechanical arm pierces the paper to identify the particle that has been measured. The computer logs the different sizes in a number of bins and displays a histogram.

The data can be re-binned as necessary depending of the spread of the data. The sizes are calibrated using the scale bar on the TEM image, provided that the TEM images all share the same magnification. A magnification of x80000 is used for nanoparticles that are 10-20 nm in diameter. This level of magnification is a good compromise between the number of particles per image and the relative difference in size of the particles. A distribution function can then be fitted to the data to determine the median particle diameter. It has been shown that the lognormal distribution is suitable for ferrofluids [51]. The lognormal distribution is a probability distribution function that applies to a continuous random variable whose natural logarithm is normally (Gaussian) distributed. Unlike the normal distribution the lognormal distribution only has non-zero values for positive, real numbers and is asymmetric. The form of the lognormal distribution is given by equation 4.2 for a linear increment of the random variable.

$$f(D)dD = \frac{1}{\sqrt{2\pi}\sigma_{\ln(D)}D} exp\left[-\frac{\left((\ln D)-\mu\right)^2}{2\sigma^2_{\ln(D)}}\right] dD \qquad (4.2)$$

Where D is the nanoparticle diameter, μ is the mean of ln(D) and $\sigma_{ln(D)}$ is the standard deviation of ln(D) and is given by equation 4.3. The term before the exponential in equation 4.2 is a normalisation parameter that forces the area under the curve to be equal to one. As a result the data needs to be normalised as a probability prior to curve fitting.

$$\sigma_{\ln(D)} = \left[\frac{1}{N}\sum(\ln D)^2 - \left(\frac{1}{N}\sum \ln D\right)^2\right]^{\frac{1}{2}} \tag{4.3}$$

In equation 4.3, N is the total number of particles measured. In order to determine the standard deviation accurately the total number of particles must be high, i.e. N>500.

Once a lognormal function has been fitted to the experimental data the sample can be characterised by its median particle diameter, D_m. The median particle diameter is defined as the value for which N/2 particles have diameters less than or equal to it and N/2 have diameters greater than or equal. The median particle diameter can be calculated from the mean of the lognormal distribution and is given by equation 4.4. An example of a lognormal fit is shown in figure 4.4.

$$D_m = exp(\mu) \tag{4.4}$$

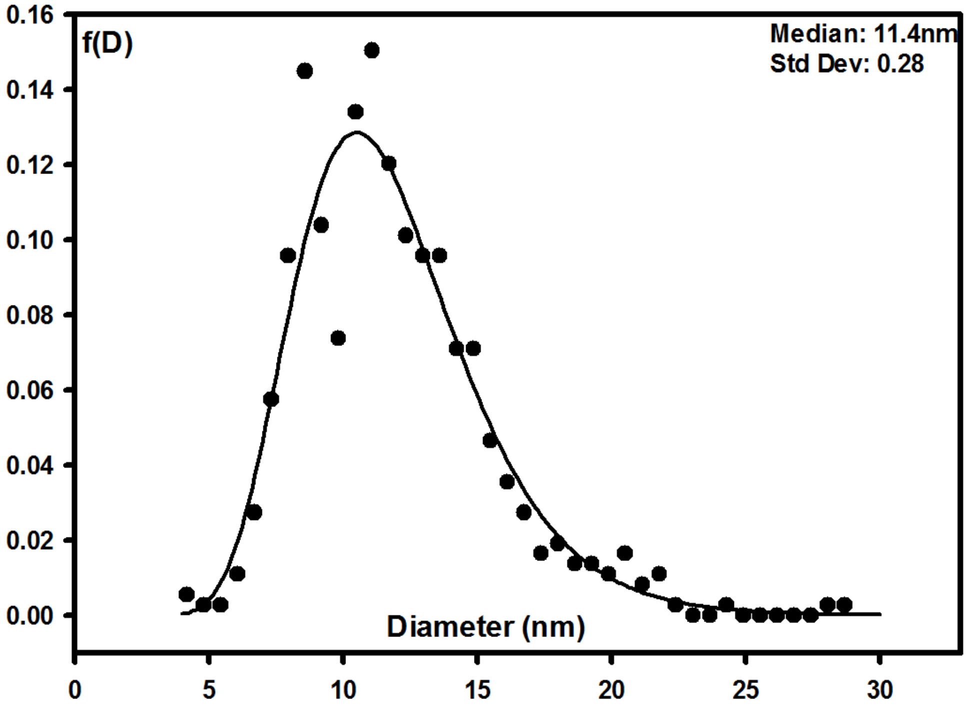

Figure 4.4: A typical lognormal distribution fitted to data for a ferrofluid sample.

4.4 Anisotropy Distributions

Experimental determination of the shape anisotropy distribution requires that the particle elongations are measured. The most effective way to do this is to use image processing software on bright field TEM (Transmission Electron Microscopy) images of the particles. The software package used in this work was ImageJ [52]. ImageJ is a Java based image processing software program developed at the National Institutes of Health (US). The software is public domain and is available free of charge.

The shape anisotropy constant of a nanoparticle is dependent upon the shape demagnetising factors of the nanoparticle. These demagnetising factors are geometric factors that are well understood for ellipsoids. The shape demagnetising factors for a prolate ellipsoid are given by equations 4.5 and 4.6 and are functions of elongation only. The elongation of a single nanoparticle is determined by its aspect ratio r, which is given as the ratio between the major axis and the minor axis as shown in figure 4.5a. The ellipsoidal shape approximation can be justified via inspection of TEM images. Smaller particles appear to be spherical and elongate (favouring a single direction) as they grow.

$$N_c = \frac{4\pi}{r^2-1}\left[\frac{r}{\sqrt{r^2-1}}\ln\left(r+\sqrt{r^2-1}\right)-1\right] \tag{4.5}$$

$$N_a = \frac{4\pi - N_c}{2} \tag{4.6}$$

To determine the distribution of aspect ratios accurately, a large number of nanoparticles need to be measured (>500). This means that the method employed needs to be both accurate and time efficient. However, the effectiveness of any image processing software is dependent on the quality of the used image. The quality of a bright field TEM image can change dramatically according to how well the optics have been aligned, contamination of both the magnetic lenses and the sample and the amount of sample drift observed. In addition the degree to which the nanoparticles are aggregated determines the extent to which the boundary between two nanoparticles can be seen. Indeed measuring the aspect ratio of a nanoparticle relies on being able to observe its edge. As a result a number of measurement methods are possible and the most reliable are described below.

The first method is the simplest and is analogous to measuring the two axes of the nanoparticles separately with a ruler. In order to measure either axis: the “straight line selection tool” is selected and a line is drawn across the nanoparticle (see figure 4.5b). For the major axis the longest possible line is chosen and for the minor axis the longest perpendicular bisector. The length of the line (in pixels) can be read off. It is helpful to zoom-in on the nanoparticle being measured to observe its edge accurately.

The next method has the user trace the outer edge of a nanoparticle in order to measure its shape. To do this the “polygon selection tool” is used and each mouse click adds another line segment to the polygon, linking the previous point and the new point. Once a particle is selected in this way (see figure 4.6a) the aspect ratio can be determined by the software. This is done by selecting measure command and the measurement will be logged. The types of measurement taken can be specified initially. Obviously the more line segments used the more accurately the polygon approximates the particle shape. The advantage of this method is that the entire edge of the nanoparticle is selected which eliminates the user error associated with determining the position of the major and minor axes. The software calculates the aspect ratio by fitting an ellipse to the nanoparticle.

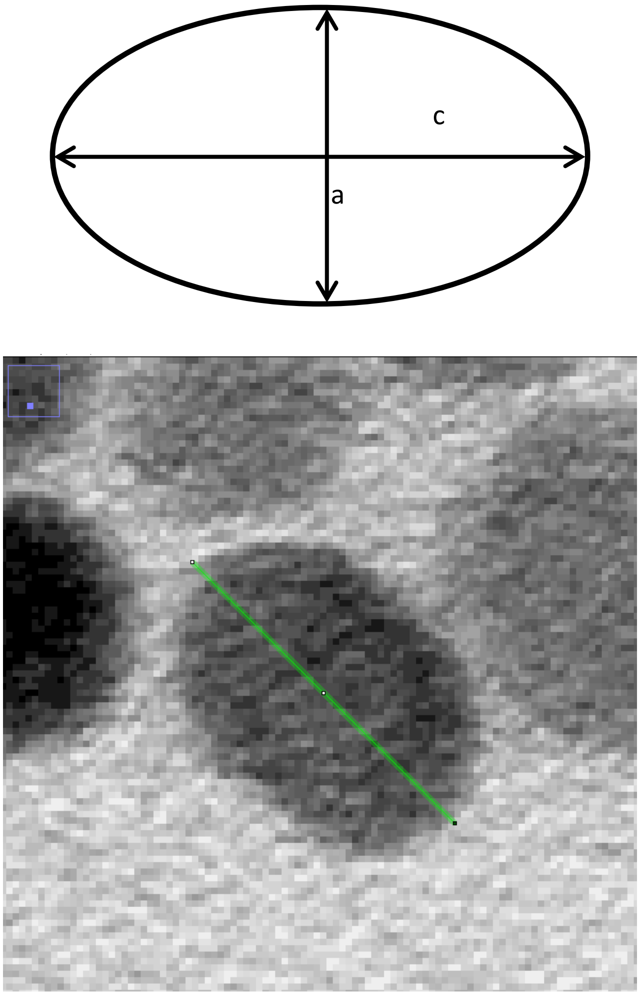

Figure 4.5: a) The aspect ratio is defined as r=c/a. b) The major axis of an elongated nanoparticle being measured using the line tool.

The final method involves making the greyscale TEM image into a binary (threshold) image as seen in figure 4.6b. This can be done when the input TEM image is of sufficient quality or the nanoparticles display white Fresnel fringes. This allows for maximum contrast between the nanoparticles and the background. This level of contrast makes it easy for the software to automatically determine the edge of the nanoparticle. The “wand tool” can be used to select a nanoparticle and a measurement of the aspect ratio can be performed as previously stated.

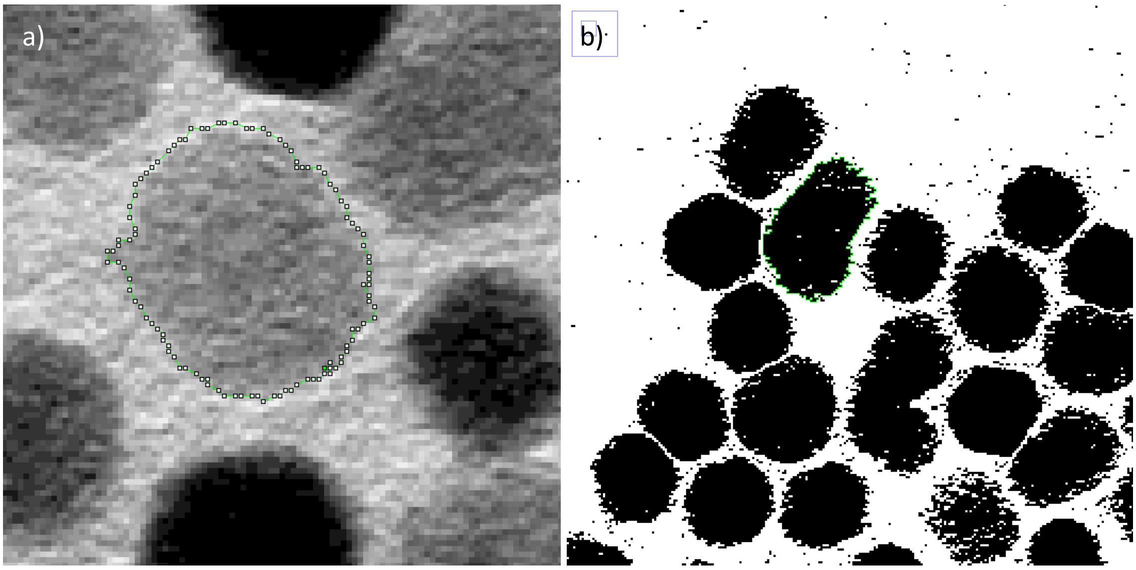

Figure 4.6: a) A nanoparticle selected using the polygon tool. b) A section of a TEM image that has been made into a binary image.

All of the methods described have their uses depending on the input image. However, for a given set of images it is important to choose the most appropriate method for the whole set to ensure consistency of measurement. The third method is the most accurate as it is mostly automated and removes user errors. Also it is efficient, as a TEM image of ~100 nanoparticles can be analysed in under a minute. However, it is not always possible to make an image binary or threshold it appropriately. Image processing software like ImageJ works by comparing pixel intensities. In images where there is strong aggregation or when the relative intensity between particle and background is comparable, it is more difficult to discern the edges. When this is the case: the image threshold process starts to change the size of the nanoparticles, making them smaller or including background in the measurement. In cases such as this, human judgement is needed to establish the boundary between nanoparticles and a method such as the second is needed.

4.5 Magnetic Measurements:

Thus far it has been assumed that the only contributions to the anisotropy are the material dependent magnetocrystalline anisotropy and the elongation dependent shape anisotropy. In order to test this assumption a measurement of the total effective anisotropy must be performed. This can be done using magnetic measurements, specifically, by observing the temperature decay of remanent magnetisation. By incorporating a second experimental approach the physical and magnetic measurements can be checked for consistency. In addition sources of anisotropy not predicted by the physical observations can be identified. The temperature decay of remanence experiment requires the use of a suitable magnetometer (section 4.5.1) and a low temperature environment (section 4.5.2).

There are size and temperature transitions between superparamagnetic and ferromagnetic behaviour. However, there is also time dependence to consider. If a sample is cooled to a low enough temperature the particles do not have sufficient time to come into thermal equilibrium. This is especially true if there is a distribution of particle sizes. If the time taken for the sample to come into thermal equilibrium is longer than the measurement time hysteresis appears and a sample of superparamagnetic particles will look ferromagnetic. Therefore, when cooling particles of a given size down to low enough temperatures it is important to consider the rate at which a sample reaches thermal equilibrium [21]. The time taken for the remanent magnetisation of a uniaxial particle to reach 1/e of its initial state is called the relaxation time, τ and is given by equation 4.7 for the case of zero applied field.

$$\frac{1}{\tau} = f_0 exp\left[-\frac{KV}{K_B T}\right] \tag{4.7}$$

Where f_0 is a frequency factor (taken as constant =10^9 Hz), K is the anisotropy constant, V is the particle volume, T is the measurement temperature and K_B is the Boltzmann constant. Equation 4.7 assumes that the initial state of magnetisation is equal to saturation. If a relaxation time of 100 seconds is chosen then equation 4.7 reduces to equation 4.8.

$$KV = 25K_B T \tag{4.8}$$

Using equation 4.8 it is trivial to see that if the volume and temperature of a particle is known then the anisotropy can be calculated. However, in a ferrofluid there is a distribution of volumes and a distribution of temperatures for which the particle magnetisations will be stable for a given τ. The latter distribution is called the blocking temperature distribution. If the median values of the volume and blocking temperature distributions are known then, by equation 4.8, the median anisotropy constant can be calculated.

The median value of the blocking temperature can be determined by observing the temperature decay of remanence. The temperature at which the remanent magnetisation drops to half its maximum value, half of the volume of the particles will be blocked. Mathematically this temperature is the median blocking temperature. This allows for an indirect determination of the effective magnetic anisotropy constant.

The measurement is performed on a raw sample of the ferrofluid. The fluid is encased in an elongated capsule with an aspect ratio of at least 1:3. This is to reduce the demagnetising effect associated with a magnetic sample in an external field (see section 4.5.1). The sample is mounted in the magnetometer and is cooled in zero-field to the lowest possible working temperature. Theoretically the maximum value of remanence is reached at absolute zero. The liquid should be allowed to freeze in zero-field to prevent any frozen-in easy axis orientations.

A saturating magnetic field is then applied to the sample. The field needed to reach the saturation magnetisation of the sample can easily be found by observing the major hysteresis loop. The external field is then removed and the magnetisation will reach its remanence point. A period of 100 seconds is left before the moment of the sample is recorded. The 100 second waiting time allows the remanence to decay by the same amount for each data point. Specifically, the 100 seconds is needed for the condition shown in equation 4.8. The temperature is then increased by a set amount and the sample space is allowed to come into thermal equilibrium. The saturating field is then re-applied and the procedure is repeated.

4.5.1 The Vibrating Sample Magnetometer (VSM):

The basis of understanding the process of magnetic nanoparticle hyperthermia lies in the magnetic behaviour of the samples. Parameters such as the saturation magnetisation, i.e. the concentration of the particles, remanence and coercivity need to be determined. Also specialised measurements such as the temperature decay of remanence (see section 4.5) need to be performed for the anisotropy to be measured. Closed coil measurement devices such as the AC susceptometer and the B-H loop tracer are inadequate as they do not produce fields high enough to saturate the ferrofluid samples. Therefore, an open coil measurement system is required. The best option is the vibrating sample magnetometer (VSM).

The VSM was originally designed by Foner in 1959 [53] (separately by [54] and [55]). The magnetometer is based upon Faraday's law of magnetic induction. The law states that a change in magnetic flux through a coil of conducting material will induce an emf in the coil. This emf is proportional to the rate of change of flux and the magnitude of the flux itself as given by equation 4.9. Where V_{ind} is the induced emf, N is the number of turns in the coil and $d\phi/dt$ is the rate of change of flux. The negative is due to Lenz's law. In the case of the VSM the source of the magnetic flux is the net magnetic moment of the sample being measured.

$$V_{ind} = -N\frac{d\Phi}{dt} \tag{4.9}$$

The VSM works by magnetising a sample in an applied field created by an electromagnet (figure 4.7). Most VSM magnets are capable of applying fields of more than 1T. The applied field is static and uniform between the pole pieces. The sample is then oscillated using a head drive. The head drive, historically, is based upon a loud speaker cone but is usually a linear actuator of some kind. The sample and the head drive assembly are kept apart by a long rigid sample rod. The position of the oscillating sample is such that it moves between a set of detection coils. As the sample oscillates the net magnetic moment creates a change in flux, which induces a voltage in the coils. This voltage is detected and the moment calculated. The process can be repeated at different values of applied field and M-H curves can be plotted in a relatively short period of time. The moment to induced emf can easily be calibrated. Calibration is done using a sample with a known moment, for example palladium and can achieve resolutions of up to $1\text{x}10^{-6}$ emu. Palladium is chosen over traditional nickel calibration samples as its moment is lower and provides a more accurate calibration.

The detection coils are arranged in pairs. Normally two pairs are used, one either side of the sample. Each coil in a pair is connected in series and counter wound, this reduces the error due to sample positioning. Both pairs are positioned coaxially such that stray field errors can be removed and non-uniformities in the applied field can be accounted for. In more advanced systems 4 pairs of detection coils are used. By placing them with their axes perpendicular to each other, angle dependent measurements can be performed.

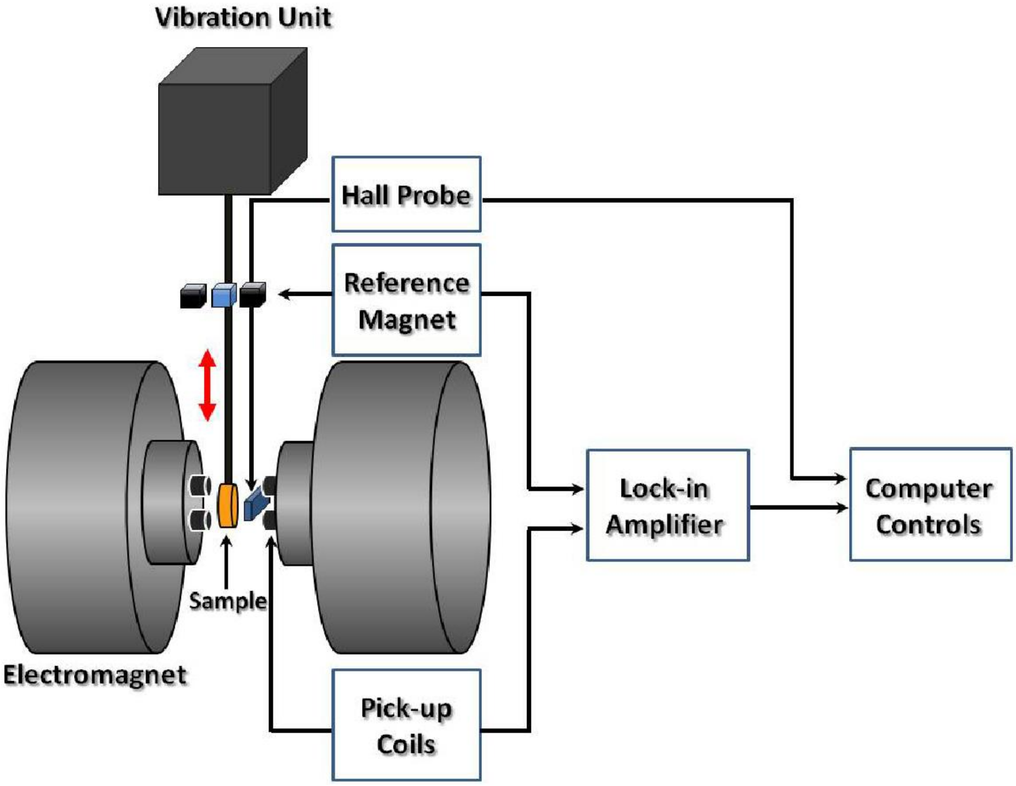

Figure 4.7: Schematic diagram of a vibrating sample magnetometer.

The head drive oscillates at a known frequency (81 Hz) generated by the controller equipment. A pair of reference coils is located in or near to the head drive. These produce a reference signal of the same frequency and amplitude as the sample. This reference signal can be added out-of-phase to the signal from the detection coils (using a lock-in amplifier) to produce a null signal. Therefore, any additional signal detected is due to the moment of the sample and any outside vibration are accounted for. More recently the role of the reference coils has been replaced by the use of piezoelectric sensors.

The applied magnetic field is generated by a pair of water cooled Helmholtz coils. The gap between the magnetic pole pieces is small enough to create a uniform field. A Gauss probe is placed in the vicinity of the pole pieces to measure the applied field. This can be used as part of a feedback system to control the field. This is an alternative to simply controlling the current through the magnet coils which does not account for remanent fields in the magnet assembly. This is especially true for superconducting magnets.

The robust design of the VSM makes it an ideal choice for performing accurate magnetic measurements. The simple arrangement of the equipment allows easy installation of cryostat and oven assemblies. This allows for magnetic measurements at a range of temperatures, down to liquid helium (~4.2K). The VSM used in this work is a Lakeshore 7400 Series VSM [56].

4.5.2 Liquid Helium Cryostat Design:

The motivation behind the temperature decay of remanence measurements is to determine the median blocking temperature of the nanoparticles. For nanoparticles of magnetite the blocking temperature will be less than 100K. Thus, for a good variation in temperature the measurements must be carried out with liquid helium. Liquid helium, used as a cryogen with an appropriate cryostat, can sustain working temperatures down to 4.2K. Cryostats used with VSMs exist in a number of configurations: they can be self-contained units or be part of the vibrating head drive if the drive is hermetically sealed. Additionally, they can expel the used cryogen gas or be connected to a recycling system. This can be advantageous when there are transport or cost issues involved.

The cryostat used in this work is an Oxford Instruments Model CF1200 [57] and modified at the University of York. A schematic diagram of the cryostat is shown in figure 4.8. It consists of a sample space in which the vibrating rod from the VSM can vibrate freely. This sample chamber is filled with an inert gas (helium) at a pressure slightly greater than atmosphere; this displaces atmospheric oxygen, nitrogen and water vapour. By displacing these gases they cannot freeze in the sample chamber at liquid helium temperatures. The top of the sample chamber consists of a silicone-rubber diaphragm seal. This seal is pliant enough that the movement of the vibrating rod is not damped but durable enough to maintain the pressure differential between the sample chamber and atmosphere.

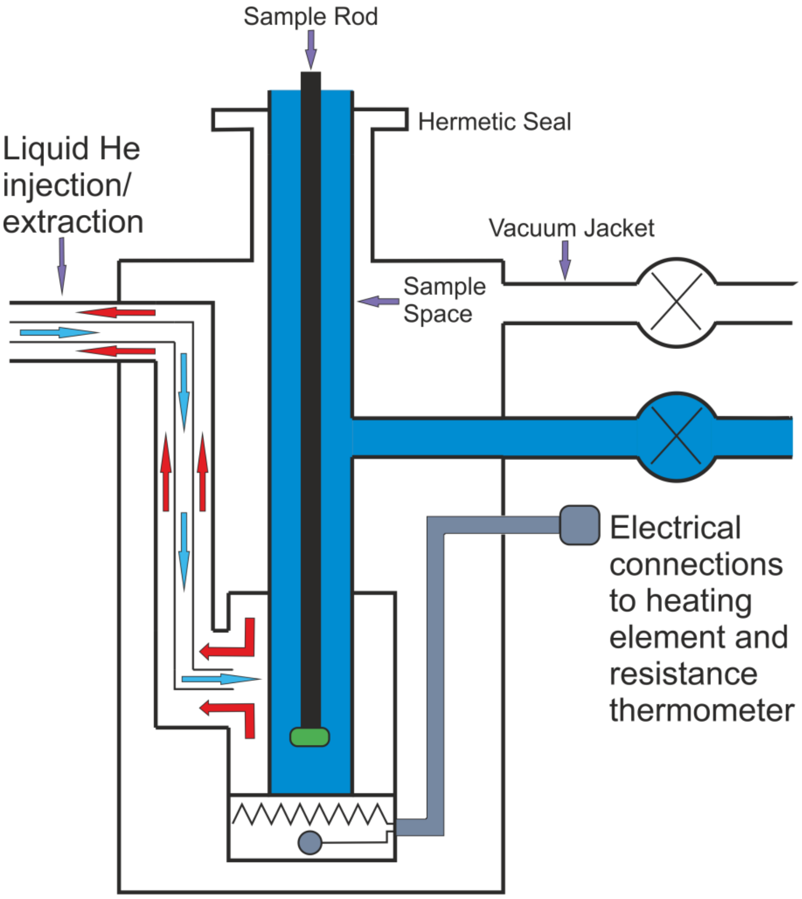

Figure 4.8: Schematic diagram of the liquid helium cryostat.

Surrounding the sample chamber is the cryogen chamber. The chamber allows liquid helium to be circulated around the sample chamber from a Dewar to a collection vessel. In this design the constantly flowing liquid helium acts as a thermal reservoir conducting heat away from the sample space. The cryogen chamber also contains a heater coil and a thermocouple. The heater coil allows the temperature to be varied accurately with the use of a PID (Proportional Integral Differential) controller. The thermocouple is attached to a copper block on the wall of the sample chamber which acts as a thermal mass, minimising temperature fluctuations. Finally, the entire assembly is surrounded by a vacuum jacket that inhibits heat transfer to the cryostat from the surroundings.

4.6 Hyperthermia Measurements:

Any model of magnetic nanoparticle hyperthermia is only valid if it is consistent with relevant heating measurements. Heating measurements were performed using a NanoTherics Magnetherm [58], shown in figure 4.9.

Figure 4.9: The NanoTherics Magnetherm used to conduct heating measurements on the ferrofluids.

The magnetherm itself consists of a changeable water-cooled coil connected to a resonance circuit. This produces an alternating magnetic field across the sample chamber. The field amplitude and frequency can be tuned by changing the size of the coil, the voltage applied across the coil and the capacitance of the resonance circuit.

The nanoparticle sample is held in a vessel that is insulated from the surrounding to prevent heat dissipation. The temperature of the sample is determined using a thermocouple immersed in the fluid. The effect of an applied field on the thermocouple can be reduced by the choice of material (nonferrous alloys) and geometry (twisted leads).

Heating measurements using the magnetherm are performed by observing the change in temperature with time. The temperature rate is dependent on the field and frequency used. The heating measurements conducted in this work were performed at a constant field amplitude and frequency of 250 Oe and 111 kHz respectively. The temperature gradient is then used to determine the specific absorption rate (SAR) of the sample, given by equation 4.10.

$$SAR = \frac{C\rho}{\Phi}\left[\frac{\Delta T}{\Delta t}\right] \tag{4.10}$$

Where C is the specific heat of the colloid, Φ is the concentration of iron in the solution, ρ is the density of the colloid and ΔT/Δt is the heating rate. It should be noted that equation 4.10 applies to the initial heating rate.

Chapter 5: Results and Discussion

The results of the experimental work conducted are presented in this chapter. For each section the key result of the experiment is presented along with additional information that could be considered relevant to the experimental procedure. In other words, specific procedures undertaken that were not discussed in chapter 4.

This chapter begins with an introduction to the samples used in the experiments and then their basic magnetic profiles are given. The distributions of the particle size and shape are presented. this leads on to the overall shape anisotropy distributions for the systems. The chapter then changes focus towards the magnetic measurements. Temperature decay of remanence experimental results are discussed in the context of an effective anisotropy. Heating measurements are presented at the conclusion of the chapter.

5.1 Sample Systems:

One ferrofluid sample is consistently used throughout the experimental work presented in this chapter. The sample is a ferrofluid containing iron oxide (magnetite and maghemite) CGP nanoparticles coated by DMSA (a hydrophilic surfactant). The particles are suspended in water.

For the remainder of this thesis the sample will be referred to as sample A. Sample A has a concentration of 20 milligrams of iron per millilitre of colloid [59]. The concentration and colloid of this sample means that it would be approved for in vivo use. For the X-ray diffraction experiments the sample was used in the form of a powder.

Nanoparticles dispersed in water are known to aggregate more readily than those dispersed in oils. Therefore, the heating measurements described in section 5.7 are performed on oil based ferrofluids. Samples D and E contain the similar sized particles as sample A [59] at a concentration of 10 milligrams of iron per millilitre of colloid. Sample D is a pure oil based ferrofluid and Sample E is dispersed in a wax. Samples B and C contain smaller particles, D_m=10.3 nm [59]. The concentrations are the same as those of samples D and E. Sample B is a pure oil based ferrofluid and Sample C is dispersed in a wax as well. In the wax particles cannot stir and the heating is purely to hysteresis heating.

5.2 Basic Characterisation:

The hysteresis of sample A was measured at T=4.2 K using a VSM and liquid helium cryostat. The M-H curve is shown by figure 5.1. A liquid sample holder was used that had an elongation of 3:1. This was used in order to reduce the contribution of the demagnetising field of the sample. Additionally, the sample was allowed to freeze in zero field to prevent frozen-in ordering of the particles.

The error in the magnetisation has been reduced by plotting the reduced magnetisation. A maximum field of 3 kOe was used and was more than sufficient to saturate the particles. The particles exhibit magnetic hysteresis and the overall magnetic profile of sample A is ferrimagnetic. The coercive field for this sample is H_C= 2.95x10^2 Oe. By inspection of figure 5.1 it can be noted that there is a deviation from the theoretical value of remanence M_R=0.5M_S.

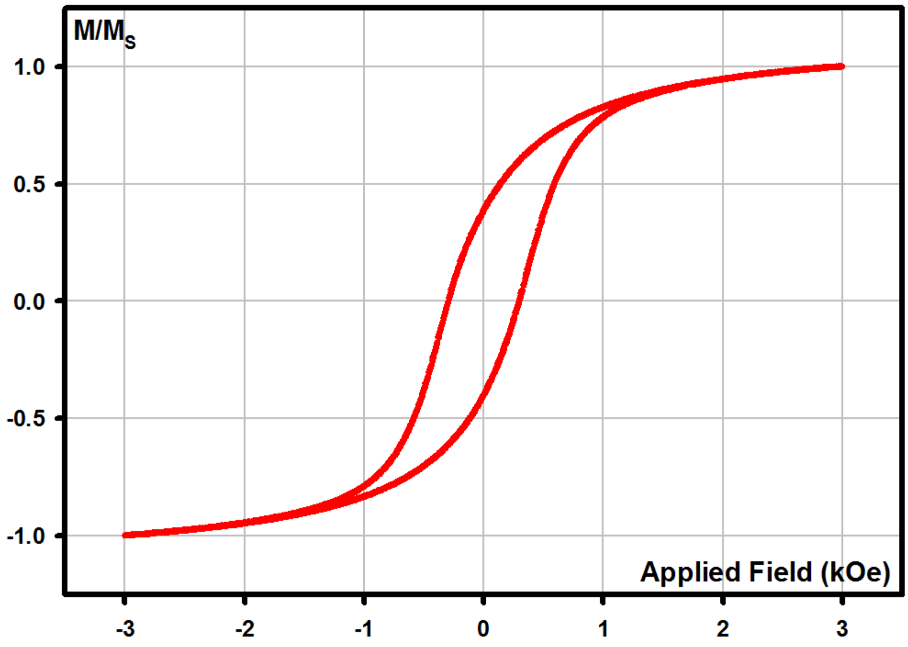

Figure 5.1: The M-H curve for sample A.

Sample A in a powder form was placed in an X-ray diffractometer in order to verify the composition of the nanoparticles. In order to reduce contamination by the magnetic particles within the diffractometer a layer of powder was held in place by a layer of double-sided tape on a glass slide. Both materials are amorphous and their contribution to the X-ray diffraction spectrum is negligible.

Figure 5.2 shows the results of the theta/2-theta scan for sample A. Since the sample was in powder form, the density of the sample along its length was not uniform. Thus, Bragg-Brentano focusing conditions were used over parallel beam. The incident slit and first receiving slit were adjusted to one quarter of a degree and the second receiving slit was narrowed to 0.1 mm to increase the resolution of the scan. The resolution achieved by this scan was 0.05 degrees.

Figure 5.2 was compared to known crystal data and the large intensity peaks observed correspond to magnetite (Fe_3O_4). The dominant peaks seen in figure 5.2 correspond to the (220), (311), (400), (422), (511) and (440) planes (left to right) for magnetite. Magnetite is taken to be the dominant phase. However, other iron oxide phases (e.g. maghemite) may be present and at this resolution quantitative phase analysis cannot be performed.

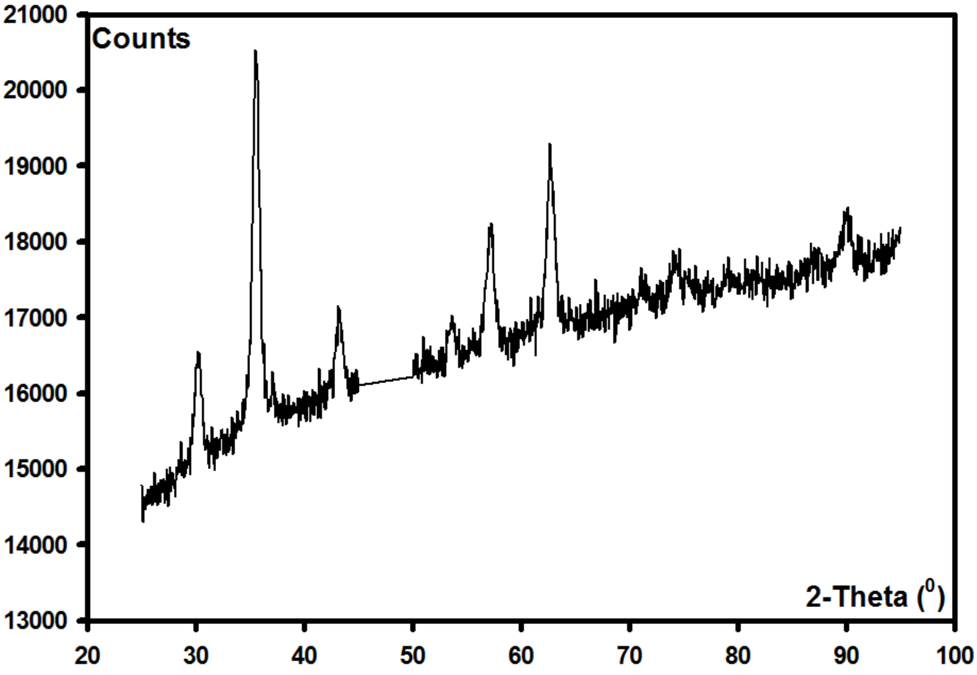

Figure 5.2: X-ray diffraction pattern for sample A using a theta/2-theta scan type.

5.3 Particle Size Analysis:

As stated in section 4.3 the size analysis is performed on TEM bright field images. A few drops of sample A were diluted in water and applied via pipette to a continuous carbon TEM grid. The dilution reduces the particles per unit area on the grid. Too many particles per unit area makes size analysis difficult. A representation TEM image is shown in figure 5.3.

Figure 5.3 reveals particles that deviate slightly from spherical shapes and a large degree of aggregation. The particles were seen to form closely packed clusters. The degree of aggregation is most likely due to the fact that sample A is a water based ferrofluid.

More than 500 particles were measured using the method described in section 4.3. Figure 5.4 shows the particle size distribution, f(D). A lognormal distribution was fitted to the data and the median particle diameter was found to be 11.4nm The standard deviation of the distribution was 0.28.

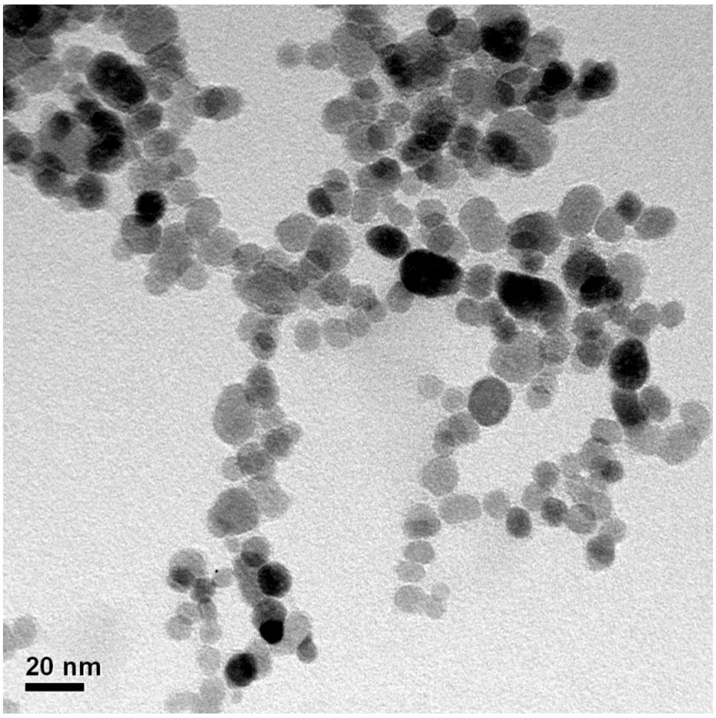

Figure 5.3: Bright field TEM micrograph of the particles in sample A.

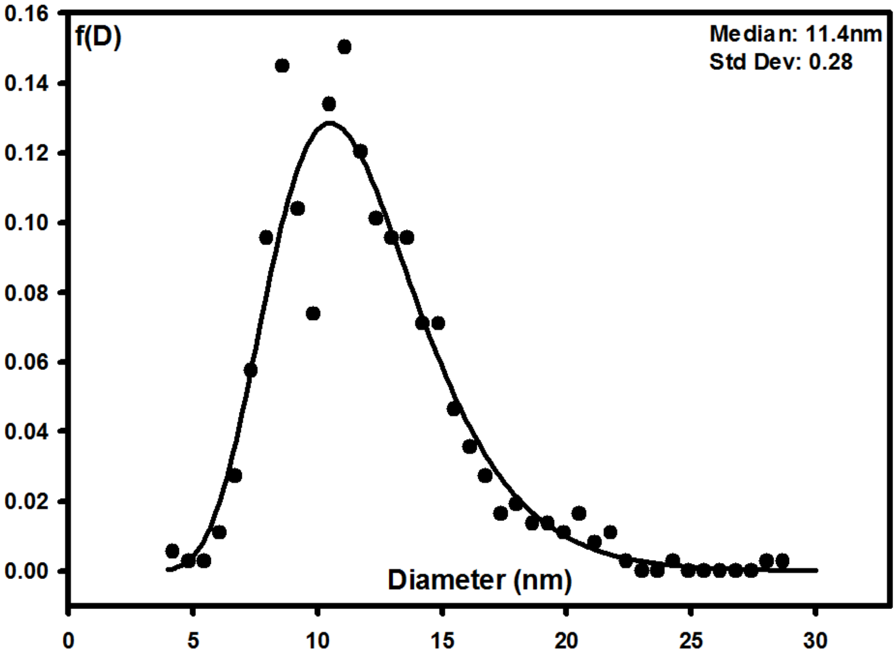

Figure 5.4: Particle size distribution for sample A.

5.4 Distribution of Particle Elongations:

Using the methodology described in section 4.4 on the TEM images the aspect ratios of over 500 particles were found. The approximation of the particles to ellipsoids was proven to be reasonable.

Figure 5.5 shows the distribution of elongations. The distribution was plotted as the aspect ratio minus 1. This was done to force the origin of the distribution to be zero and the lognormal distribution was found to be a more accurate fit in this case. Thus, a median aspect ratio of r=1.17 was found and the standard deviation of the distribution 0.71. As predicted in section 3.3 all of the particles have aspect ratios in the range 1.0 to 2.0. Although, the distribution is quite narrow a significant variety in the shape anisotropy will occur.

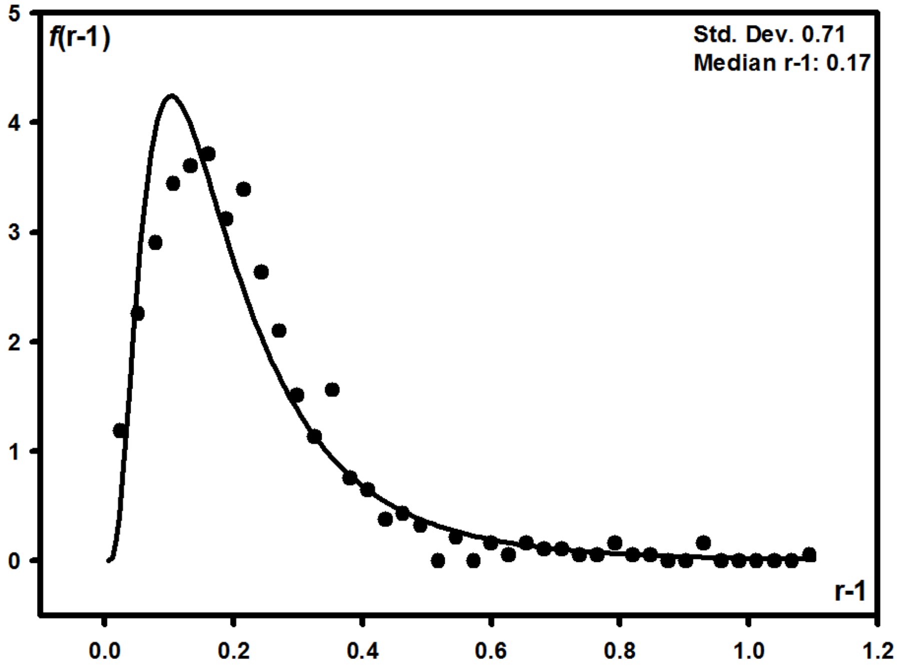

Figure 5.5: Particle elongation distribution for sample A.

5.5 Calculation of Anisotropy Distribution:

The values of the aspect ratio for the particles measured in section 5.4 were converted to anisotropy constants. Figure 5.6 shows the distribution of anisotropy constants. K_S values range from 0.1x10^5 erg/cc to 3.6x10^5 erg/cc.

As predicted in section 3.3 the shape anisotropy distribution is significant, even for the narrow distribution of elongations show by figure 5.5. The anisotropy distribution appears to be lognormal and by assuming this distribution a median value of the shape anisotropy, K_S=0.9x10^5 erg/cc was found with a standard deviation of the lognormal distribution equal to 0.64.

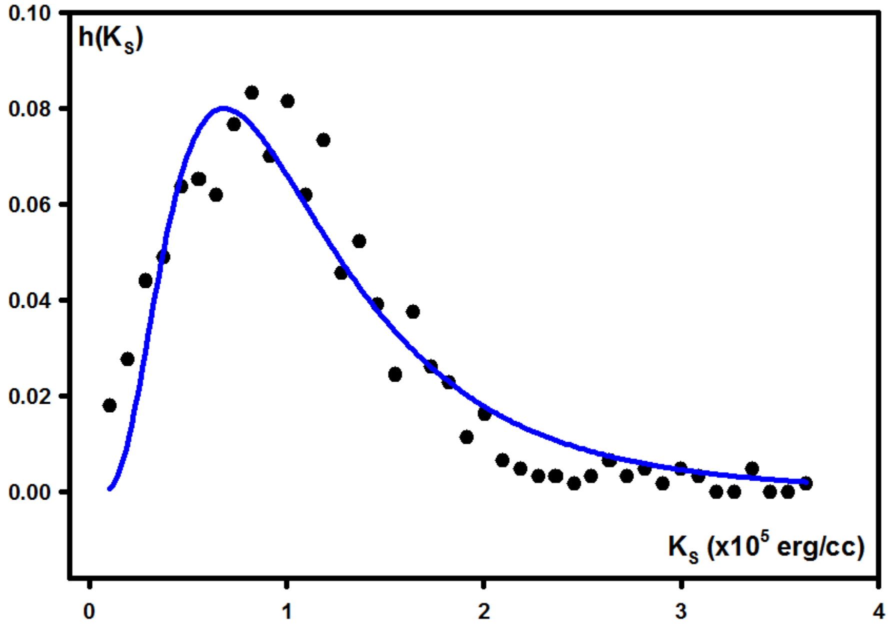

Figure 5.6: The shape anisotropy distribution for sample A.

5.6 Temperature Decay of Remanence:

The temperature decay of remanence was performed using a VSM and a liquid helium cryostat. The experimental methodology used was that expressed in section 4.5. A liquid sample holder with an elongation ratio of 3:1 was used to minimise the effect of the demagnetising field and the ferrofluid was allowed to freeze in zero field. Rather than sweeping the temperature, the temperature was set for a specific value and the system was left to come into thermal stability before conducting the remanence measurement. The field was increased to H=5 kOe to ensure that the sample was magnetically saturated. The field was removed and a time of 100 seconds was left before the measurement was logged.

Figure 5.7 shows the temperature decay of remanence curve for sample A. The magnetisation axis has been normalised to M_R(max). This is the value the remanence would have at T=0 K and was found by extrapolation. As described in section 4.5, the temperature at which the remanent magnetisation drops to half of its original values is the median blocking temperature. T_{Bm}= 46 K from figure 5.7 and using equation 5.1 the median value the total anisotropy was found.

$$K_m = \frac{150 K_B T_{Bm}}{\pi D_m^3} \tag{5.1}$$

Where 150 comes from the 25 in equation 4.8 for the energy barrier and $V=\pi D^3/6$. From equation 5.1 the anisotropy value $k=2.1\text{x}10^5$ erg/cc was found.

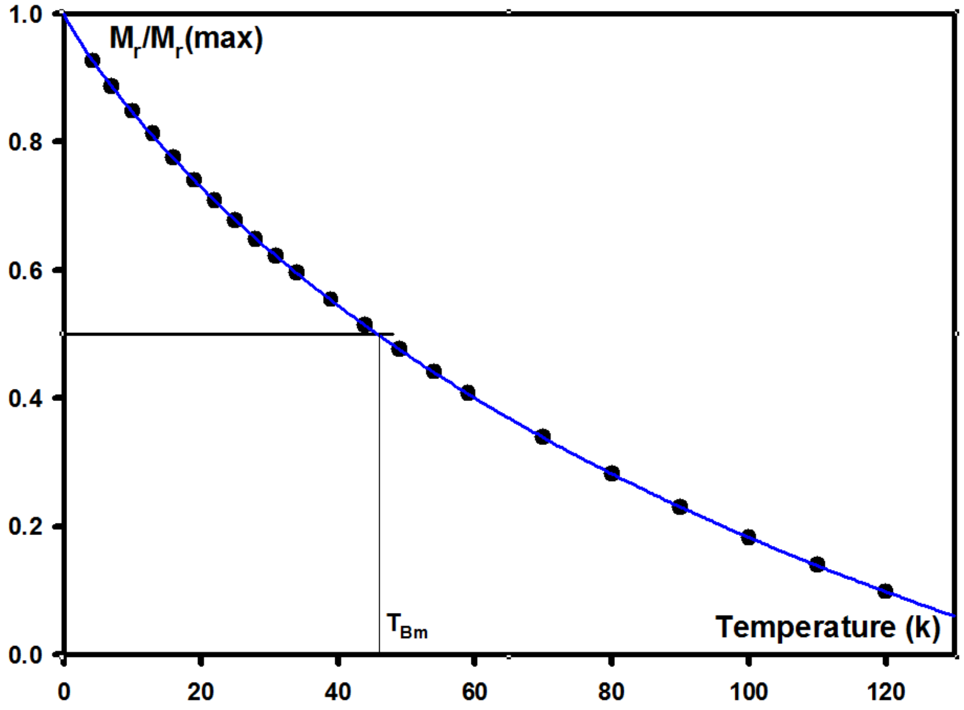

Figure 5.7: The temperature decay of remanence curve for sample A.

The blue line in figure 5.7 comes from a computational fit of the particle size distribution shown in section 5.3 to the temperature decay of remanence data [60]. Using the values of D_m and $\sigma_{ln(D)}$ from figure 5.4 the standard deviation of the anisotropy distribution was found to be $\sigma_{ln(K)}$=0.2.

5.7 Hyperthermia Measurements:

Since the degree of aggregate particles found in water based ferrofluids and demonstrated by figure 5.3 heating measurements on sample A were impractical. The heating measurements shown by figure 5.8 were conducted on samples B-E. Since this is a comparative study, heating induced in the thermocouple is constant between results and is neglected.

In figure 5.8, red circles indicate sample B, blue circles sample C, red triangles sample D and blue triangles sample E. Assuming that a smaller particle size distribution results in a narrower shape distribution. A narrower shape anisotropy distribution will exist and the anisotropy more closely approximates a single value. This can be seen in figure 5.8 by the two heating curves for samples D and E. However, for samples B and C which are larger, the anisotropy distribution is larger. The effect of the large anisotropy distribution is to force the heating curves further apart.

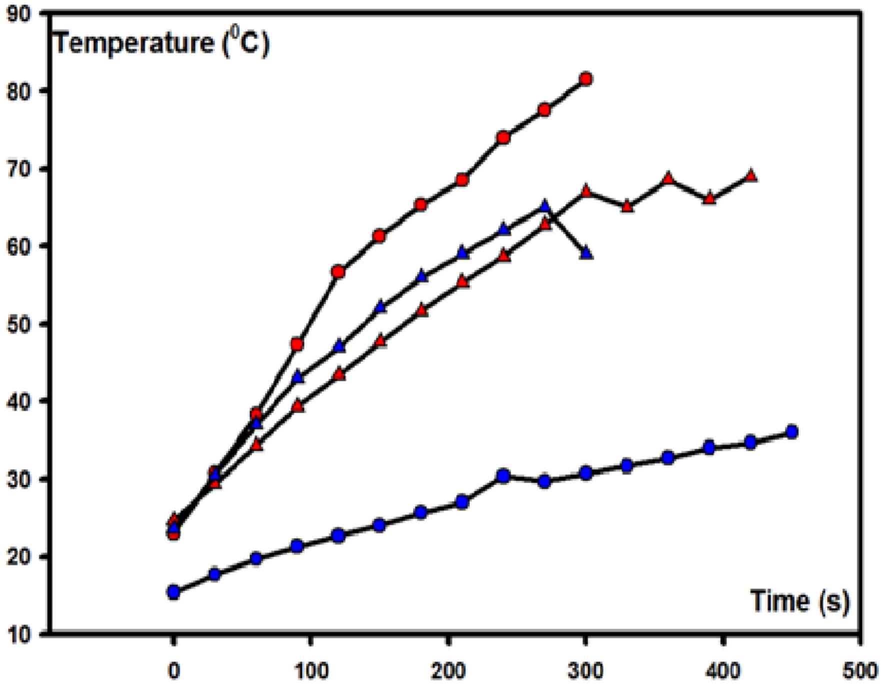

Figure 5.8: Heating measurements for samples B-E, dispersed in oil and wax.

Chapter 6: Conclusions and Future Work

6.1 Conclusions:

From the outset the aim of this work was to determine if a shape anisotropy distribution could be generated and if so would the distribution be significant. A method for determining the shape anisotropy distribution for TEM images formed and the distribution was indeed calculated and shown to be lognormal in form.

Section 5.5 has shown that even for a relatively narrow distribution of particles sizes in the range of 1 to 2, the distribution of anisotropy constants is significant. Therefore, it has been experimentally proven that consideration of the anisotropy distribution is needed for an accurate model of magnetic hyperthermia, especially for medical applications. Thus models assuming a constant anisotropy value and a spherical particle shape will never predict accurate heating rates.

A puzzling issue has been raised from the magnetic measurements in section 5.6. The median value for the shape anisotropy is significantly lower than the value of the median, effective anisotropy constant calculated from the remanence curve. Additionally, the spread of the anisotropy distribution, related to $\sigma_{\ln(K)}$, is not in agreement between the two methods. This discrepancy is significant even if the magnetocrystalline anisotropy is included with the shape anisotropy. This difference in value suggests another contribution to the energy barrier involved. Whether this is related to the large number of aggregates present in the sample studied herein is yet to be determined.

6.2 Future Work:

The remanence data in this thesis is limited and further studies will be needed to provide conclusive results. One approach for further study could be extend the experimental methodology described herein to compare oil and water ferrofluids and solid matrix assemblies of nanoparticles.

The effect of particle aggregation also need to be studied in depth as agglomerating processes will occur in the laboratory and in vivo. Therefore, a further study is required to account for the altered heating effects produced.

List of Abbreviations and Symbols

C	...	Specific heat
CCD	...	Charged coupled device
CGP	...	Controlled growth process
D	...	Particle diameter
d	...	Lattice plane spacing
D_m	...	Median particle diameter
$D_P(0)$	...	Critical diameter for susceptibility heating
$D_P(H)$	...	Critical diameter for hysteresis heating
D_S	...	Critical diameter for transition from Néel relaxation to Brownian rotation
$d\phi/dt$	...	Rate of change of magnetic flux
E	...	Total energy
E_A	...	Anisotropy energy
E_H	...	Potential energy of magnetic field
emf	...	electromotive force
E_{ms}	...	Magnetostatic energy
f	...	Frequency of measurement
f(D)	...	Lognormal distribution of particle diameters
f(V)	...	Lognormal distribution of particle volumes
f(y)	...	General lognormal distribution for parameter y
f_0	...	Frequency factor
g(K)	...	Lognormal distribution of anisotropy constants
H	...	Applied magnetic field strength
H_C	...	Coercive field
h_C	...	Reduced coercive field
$H_C(D)$	...	Size dependent coercive field
H_K	...	Anisotropy field
K	...	Anisotropy constant
K_B	...	Boltzmann constant
K_C	...	Magnetocrystalline anisotropy constant
K_m	...	Median anisotropy constant
K_S	...	Shape anisotropy constant
K_α	...	K-alpha emission line from copper
K_β	...	K-beta emission line from copper
L_C	...	Critical crystal length for single magnetic domains
M	...	Magnetisation
m	...	Reduced magnetisation
M_R	...	Remanent magnetisation
M_S	...	Saturation magnetisation
n	...	Diffraction order
N	...	Number of turn in a wire coil
N_a	...	Shape demagnetising factor along minor axis of an ellipsoid
N_c	...	Shape demagnetising factor along major axis of an ellipsoid
N_d	...	Shape demagnetising factor
P_{ac}	...	Power from susceptibility heating
P_{hys}	...	Power from hysteresis heating
PID	...	Proportional-integral-differential controller
PMT	...	Photomultiplier tube
R	...	Field sweep rate
r	...	Particle aspect ratio
SAR	...	Specific absorption rate
T	...	Temperature

t	...	Time
T_B	...	Blocking temperature
T_{Bm}	...	Median blocking temperature
t_{eff}	...	Effective measurement time for an alternating magnetic field
TEM	...	Transmission electron microscopy
V	...	Volume
V_{ind}	...	Induced emf
V_P	...	Critical volume for superparamagnetic behaviour
VSM	...	Vibrating sample magnetometer
y_m	...	Median value of variable in lognormal distribution
α	...	Angle between a particles easy axis and an applied field
γ_D	...	Domain wall energy
ΔE	...	Energy barrier
$\Delta T/\Delta t$	...	Heating rate
η	...	Viscosity
θ	...	Angle between a particles easy axis and its magnetisation vector
θ_{Scat}	...	Scattering angle
λ	...	Wavelength
μ	...	Mean of ln(D)
ρ	...	Density
σ	...	Standard deviation of the lognormal distribution
$\sigma_{\ln(K)}$	...	Standard deviation of ln(K)
$\sigma_{\ln(D)}$	...	Standard deviation of ln(D)
τ_B	...	Brownian relaxation time
τ_N	...	Néel relaxation time
τ_{Tot}	...	Combined relaxation time for Néel and Brownian relaxation
χ	...	Initial DC susceptibility
χ''	...	Complex part of the AC susceptibility

References:

[1] W. C. Dewey, L. E. Hopwood, S. A. Sapareto, L. E. Gerweck, Radiology, **123(2)** (1977), 463–474

[2] S. J. DeNardo, G. L. DeNardo, A. Natarajan, et al., Journal of Nuclear Medicine, **48(3)** (2007), 437–444

[3] P. Wust, U. Gneveckow, M. Johannsen, et al., International Journal of Hyperthermia, **22(8)** (2006), 673–685

[4] P. C. Scholten, J. Magn. Magn. Mater., **39(1-2)** (1983), 99–106

[5] H. Mamiya, I. Nakatani, T. Furubayashi, Phys. Rev. Letts., **80(1)** (1998), 177–180

[6] H. Mamiya, I. Nakatani, T. Furubayashi, Phys. Rev. Letts., **82(21)** (1999), 4332–4335

[7] H. Mamiya, I. Nakatani, T. Furubayashi, Phys. Rev. Letts., **84(26)** (2000), 6106–6109

[8] X. M. Lin, A. C. S. Samia, J. Magn. Magn. Mater., **305(1)** (2006), 100–109

[9] A. H. Lu, E. L. Salabas, F. Schüth, Angewandte Chemie., **46(8)** (2007), 1222–1244

[10] The International Commission on Non-Ionizing Radiation Protection, Health Physics, **74(4)** (1998), 494–522

[11] M. Johannsen, et al, Int. J. Hyperthermia, **21** (2005), 637

[12] T. Kobayashi, Biotechnology Journal, **6(11)** (2011), 1342–1347

[13] B. Thiesen, A. Jordan, International Journal of Hyperthermia, **24(6)** (2008), 467–474

[14] J. Carrey, B. Mehdaoui, M. Respaud, J. Appl. Phys., **109** (2011), 083921

[15] P. Weiss, Compt. Rend., **143** (1906), 1136

[16] J. Frenkel and J. Dorfman, Nature, **126** (1930), 274

[17] W. C. Elmore, Phys. Rev., **54** (1938), 1092

[18] C. Kittel, Phys. Rev., **70(11-1)** (1946), 965

[19] R. F. Butler and S. K. Banerjee, J. Geophys. Res., **80(29)** (1975), 4049–4058

[20] I. S. Jacobs, C. P. Bean, Phys. Rev., **100** (1955), 1060

[21] B. D. Cullity, C. D. Graham, Introduction to Magnetic Materials, Wiley, 2nd edition (2009)

[22] L. Néel, Compt. Rend., **228** (1949), 664

[23] M.I. Shliomis, Usp. Fiz. Nauk, **112** (1974), 427, (Sov. Phys. Usp., **17** (1974), 153)

[24] E. C. Stoner, E. P. Wohlfarth, Phil. Trans. Roy. Soc., **4240** (1948), 599

[25] I. Eisenstein, A. Aharoni, Phys. Rev., **B16(3)** (1977), 1278

[26] M. Walker, P. I. Mayo, K. O'Grady, S. W. Charles, R. W. Chantrell, Phys. Condens. Matter, **5** (1993), 2779

[27] C. P, Bean, J. D. Livingston, J. Appl. Phys., **30** (1959), s120

[28] M. P. Sharrock, IEEE Trans. Magn., **26** (1990), 193-197

[29] R. W. Chantrell, G. N. Coverdale, K. O'Grady, J. Phys. D: Appl. Phys., **21** (1988), 1469

[30] M. El-Hilo, A. M. De Witte, K. O'Grady, J. Magn. Magn. Mater.,**117** (1992), 307-310

[31] F. Burrows, MSc Thesis, The University of York, UK, 2012

[32] A. Brezovich, Medical Physics Monograph, (P. R. Palival, F. W. Hetzel), American Institute of Physics, New York (1988), 82-111

[33] A. E. Deatsch, B. A. Evans, J. Magn. Magn. Mater., **354** (2014), 163-172

[34] G. Vallejo-Fernandez, et al, J. Phys. D: Appl. Phys., **46** (2013), 312001

[35] G. Vallejo-Fernandez, K. O'Grady, Appl. Phys. Lett., **103** (2013), 142417

[36] W. J. Atkinson, I. A. Brezovich, D. P. Chakraborty, IEEE Trans. Biomed. Eng., **31** 1984, 70

[37] Q. A. Pankhurst, J. Connolly, S. K. Jones, J. Dobson, J. Phys. D: Appl. Phys., **36** (2003), R167

[38] F. E. Luborsky, J. Appl. Phys., **32** (1961), S171

[39] R. Hergt, et al, J. Magn. Magn. Mater., **293** (2005), 80

[40] M. A. Gonzalez-Fernandez, et al, J. Sol. State Chem., **182** (2009), 2779

[41] C. G. Granquist, R. A. Burhman, J. Appl. Phys., **47** (1976), 5

[42] Liquids Research Limited, http://www.liquidsresearch.co.uk

[43] S. E. Khalafalla, G. W. Reimens, IEEE Trans. Magn., **16** (1980), 178

[44] M. Knoll, E. Ruska, Contribution to geometrical electron optics, Ann. Physik, **12** (1932), 607-661

[45] M. Knoll, E. Ruska, The electron microscope, Z. Physik, **78** (1932), 318-339

[46] JEOL Ltd, http://www.jeol.co.jp/en/products/list_tem.html

[47] D. Chescoe, P. J. Goodhew, The Operation of Transmission and Scanning Electron Microscopes, Oxford University Press, (1990)

[48] Rigaku Corp., http://www.rigaku.com/products/xrd/smartlab

[49] D. K. Bowen, B. K. Tanner, High Resolution X-ray Diffractometry and Topography, Taylor and Francis, (1998), 15

[50] B. D. Cullity, S. R. Stock, Elements of X-ray Diffraction, Prentice Hall, 3rd edition (2001), 207-208

[51] K. O'Grady, A. Bradbury, Journal of Magnetism and Magnetic Materials, **39** (1983), 91-94

[52] ImageJ, http://imagej.nih.gov/ij/

[53] S. Foner, Rev. Sci. Instrum., **30** (1959), 548-557

[54] G. W. Van Oosterhout, Appl. Sci. Res., **B6** (1956), 101

[55] P. J. Flanders, IEEE Special Publication **T-91**, Conference on Magnetism and Magnetic Materials, Boston, (1956), 315-317

[56] Lake Shore Cryotronics Inc., http://www.lakeshore.com/products/Vibrating-Sample-Magnetometer/7400-Series-VSM/Pages/Overview.aspx

[57] Oxford Instruments Plc., http://www.oxford-instruments.com/

[58] NanoTherics Ltd., http://www.nanotherics.com/magnetherm.htm

[59] Private Communication, J. Timmis

[60] Private Communication, G Vallejo-Fernandez